The clustering of galaxies in the completed SDSS-III Baryon Oscillation Spectroscopic Survey: anisotropic galaxy clustering in Fourier space

Florian Beutler,[1,2]★ Hee-Jong Seo,[3] Shun Saito,[4,5] Chia-Hsun Chuang,[6,7]
Antonio J. Cuesta,[8] Daniel J. Eisenstein,[9] Héctor Gil-Marín,[10,11] Jan Niklas Grieb,[12,13]
Nick Hand,[14] Francisco-Shu Kitaura,[7] Chirag Modi,[15] Robert C. Nichol,[1]
Matthew D. Olmstead,[16] Will J. Percival,[1] Francisco Prada,[6,17,18] Ariel G. Sánchez,[12]
Sergio Rodriguez-Torres,[6,17] Ashley J. Ross,[1,10] Nicholas P. Ross,[20]
Donald P. Schneider,[21,22] Jeremy Tinker,[23] Rita Tojeiro[24]
and Mariana Vargas-Magaña[25]

Affiliations are listed at the end of the paper

ABSTRACT

We investigate the anisotropic clustering of the Baryon Oscillation Spectroscopic Survey (BOSS) Data Release 12 sample, which consists of 1 198 006 galaxies in the redshift range $0.2 < z < 0.75$ and a sky coverage of $10\,252\,\mathrm{deg}^2$. We analyse this data set in Fourier space, using the power-spectrum multipoles to measure redshift-space distortions simultaneously with the Alcock–Paczynski effect and the baryon acoustic oscillation scale. We include the power-spectrum monopole, quadrupole and hexadecapole in our analysis and compare our measurements with a perturbation-theory-based model, while properly accounting for the survey window function. To evaluate the reliability of our analysis pipeline, we participate in a mock challenge, which results in systematic uncertainties significantly smaller than the statistical uncertainties. While the high-redshift constraint on $f\sigma_8$ at $z_{\rm eff} = 0.61$ indicates a small ($\sim$1.4σ) deviation from the prediction of the *Planck* ΛCDM (Λ cold dark matter) model, the low-redshift constraint is in good agreement with *Planck* ΛCDM. This paper is part of a set that analyses the final galaxy clustering data set from BOSS. The measurements and likelihoods presented here are combined with others in Alam et al. to produce the final cosmological constraints from BOSS.

Key words: gravitation – surveys – cosmological parameters – cosmology: observations – dark energy – large-scale structure of Universe.

1 INTRODUCTION

Clustering in the matter density field carries an enormous amount of information about cosmological parameters. The growth of the matter clustering amplitude is directly sensitive to the sum of the neutrino masses (e.g. Lesgourgues & Pastor 2006; Beutler et al. 2014b), the dark energy equation of state and the nature of Gravity (Kaiser 1987; Peacock et al. 2001; Guzzo et al. 2008). Galaxy redshift surveys sample the underlying matter density field with galaxies as tracer particles. A measurement of the matter clustering amplitude, σ_8, could be compared to the precise measurement

of the matter clustering amplitude at the recombination redshift, measured in the cosmic microwave background providing a long lever-arm with which to test the growth of structure. The formation of galaxies is correlated with the underlying density field, but the galaxy formation processes are complicated and do not allow us to infer these correlations from first principles. That is, while the clustering amplitude of the galaxy density field can be measured to percent level precision, it cannot straightforwardly be related to the clustering amplitude of the matter density field due to the uncertainties in the bias relation.

Despite these limitations, galaxy redshift surveys still allow constraints on the matter clustering amplitude due to redshift-space distortions (RSD). RSD are caused by the underlying peculiar velocity field along the line of sight that Doppler-shifts the features in the spectral energy distribution of a galaxy. If the redshift is

used to estimate the distance to the galaxy using Hubble's law, peculiar velocity contributions to the redshift introduce errors in the physical coordinates along the line of sight. Since it is nearly impossible to estimate the line-of-sight peculiar velocities of millions of galaxies individually, with a precision anywhere near the redshift uncertainty, rather than correcting the effect in the redshift measurements, we account for the resulting statistical distortions in the observed clustering signal.

Peculiar velocities trace the gravitational potential field, itself produced by the underlying matter density field. Therefore, the distortion effect due to the peculiar velocity field is correlated with the density field. Since the peculiar velocity field affects only the line-of-sight positions without affecting the angular positions, the distortions generate anisotropy in the observed clustering. In the linear regime, RSD lead to an angle-dependent increase in the power-spectrum amplitude of $(1 + \beta\mu^2)^2$ (Kaiser 1987), where μ is the cosine of the angle to the line of sight and $\beta = f/b$ is the growth rate f divided by the galaxy bias b. Using the angular dependence of the RSD signal, we can constrain the parameter combination $f(z)\sigma_8(z)$. The RSD signal is now considered one of the most powerful observables in large-scale structure (Peacock et al. 2001; Hawkins et al. 2003; Tegmark et al. 2006; Guzzo et al. 2008; Yamamoto, Sato & Huetsi 2008; Blake et al. 2011; Beutler et al. 2012; Reid et al. 2012; Chuang et al. 2013; Samushia et al. 2013; Nishimichi & Oka 2014).

Another source of anisotropy in the galaxy clustering signal is known as the AP effect (Alcock & Paczynski 1979). The AP effect is imprinted in the clustering measurement when converting from observable (redshifts and angles) to physical coordinates, which requires a fiducial cosmology. If that fiducial cosmology deviates from the true cosmology, it distorts the clustering signal differently along the line of sight and in angular scales. The two effects would be difficult to separate with a featureless power spectrum. By measuring the distortion in the distinct baryon acoustic oscillations (BAO) feature present in the power spectrum, we can constrain the AP signal, thereby isolating the anisotropy in the clustering amplitude due to the RSD (Ballinger, Peacock & Heavens 1996; Matsubara & Suto 1996; Okumura et al. 2008; Padmanabhan & White 2008). The AP test through the BAO signal constrains the geometry, i.e. $D_V(z)/r_s(z_d)$ and $F_{AP}(z) = (1 + z)D_A(z)H(z)/c$, where $D_V(z) = [(1 + z)^2 D_A^2(z)cz/H(z)]^{1/3}$ is the angle averaged distance depending on the angular diameter distance $D_A(z)$ and the Hubble parameter $H(z)$.

In this paper, we use the final data release (Alam et al. 2015, Data Release 12 – DR12) of the Baryon Oscillation Spectroscopic Survey (BOSS; Dawson et al. 2013), the largest galaxy redshift data set available to date to measure the anisotropy in the galaxy power spectrum. Our analysis framework follows our DR11 analysis (Beutler et al. 2014a) with several modifications: (1) in addition to the monopole and quadrupole we now include the hexadecapole, (2) we modified the fitting range to $k = 0.01$–$0.15\,h\,{\rm Mpc}^{-1}$ for the monopole and quadrupole and $k = 0.01$–$0.10\,h\,{\rm Mpc}^{-1}$ for the hexadecapole, (3) we modified our method to include the effect due to the discrete k-space grid when estimating the power spectrum, (4) we use a computationally more efficient way to include window-function effects, (5) we use larger k-bins to reduce the noise in the covariance matrix estimation, (6) we use a new set of mock catalogues called MultiDark-patchy, which have been introduced in Kitaura et al. (2016) and (7) we employ the Fast Fourier Transform (FFT) based power-spectrum estimator suggested by Bianchi et al. (2015) and Scoccimarro (2015) instead of the $\mathcal{O}(N^2)$ algorithm we used previously to speed up the computation.

Our companion paper, Beutler et al. (2016b), presents a BAO-only analysis, where we use the same power-spectrum multipole measurements, but isolate the BAO signal by marginalizing over the shape of the power spectrum (including RSD). While the BAO-only analysis does not capture the information on RSD, it will allow measurements of $D_V(z)/r_s(z_d)$ and $F_{AP}(z) = (1 + z)D_A(z)H(z)/c$ that do not depend on our understanding of RSD. Without the need to model RSD in detail, the BAO-only analysis can use a wider range of wavenumbers ($k_{max} = 0.3\,h\,{\rm Mpc}^{-1}$), and improve the BAO signal by using the BAO reconstruction technique (Eisenstein et al. 2007). BAO measurements obtained using the monopole and quadrupole correlation functions are presented in Ross et al. (2016), while Vargas-Magana et al. (2016) diagnose the level of theoretical systematic uncertainty in the BOSS BAO measurements. Beside this paper, there are three more measurements of the growth of structure (Grieb et al. 2016; Sanchez et al. 2016; Satpathy et al. 2016). Alam et al. (2016) combine the results of these seven papers (including this work) into a single likelihood that can be used to test cosmological models.

This paper is organized as follows: Section 2 presents the BOSS data set used in this analysis. Section 3 describes the power-spectrum estimator, followed by the treatment of the window function in Section 4. Section 5 introduces our power-spectrum model, which is based on renormalized perturbation theory. Section 6 discusses the mock catalogues used to derive covariance matrices for our measurements. In Section 7, we use these mock catalogues as well as *N*-body simulations to test our power-spectrum model. The analysis together with the fitting results is presented in Section 8, while Section 9 discusses the result and compares with previous studies. We conclude in Section 10.

The fiducial cosmological parameters, which we use to turn the observed angles and redshifts into comoving coordinates and to generate our linear power-spectrum models as an input for the power-spectrum templates, follow a flat ΛCDM (Λ cold dark matter) model with $\Omega_m = 0.31$, $\Omega_b h^2 = 0.022$, $h = 0.676$, $\sigma_8 = 0.8$, $n_s = 0.96$, $\sum m_\nu = 0.06\,{\rm eV}$ and $r_s^{\rm fid}(z_d) = 147.78\,{\rm Mpc}$.

2 THE BOSS DR12 DATA SET

The BOSS is part of Sloan Digital Sky Survey (SDSS)-III (Eisenstein et al. 2011; Dawson et al. 2013) and measured spectroscopic redshifts of 1198 006 million galaxies using the SDSS multifibre spectrographs (Bolton et al. 2012; Smee et al. 2013). The galaxies are selected from multicolour SDSS imaging (Fukugita et al. 1996; Gunn et al. 1998, 2006; Smith et al. 2002; Doi et al. 2010).

The survey is optimized for the measurement of the BAO scale and hence covers a large cosmic volume with a density of $\bar{n} \approx 3 \times 10^{-4}\,h^3\,{\rm Mpc}^{-3}$, high enough to ensure that shot noise is not the dominant error contribution at the BAO scale. Most BOSS galaxies are red with a prominent 4000 Å break in their spectral energy distribution; this feature allows a reliable redshift detection with a short exposer, providing a fast survey speed.

The BOSS DR12 sample covers a redshift range of $0.2 < z < 0.75$ over 10 252 deg^2 divided in two patches on the sky. The North Galactic Cap (NGC) contains 864 924 galaxies and the South Galactic Cap (SGC) contains 333 082. Although the BOSS galaxy sample consists of two separate selection algorithms, the so-called LOWZ and CMASS, we utilize the whole galaxy sample by combining these two samples. We refer to Reid et al. (2016) for concrete definitions of selection criteria for LOWZ and CMASS. The completeness of this sample in terms of stellar mass is studied in Leauthaud et al. (2016)
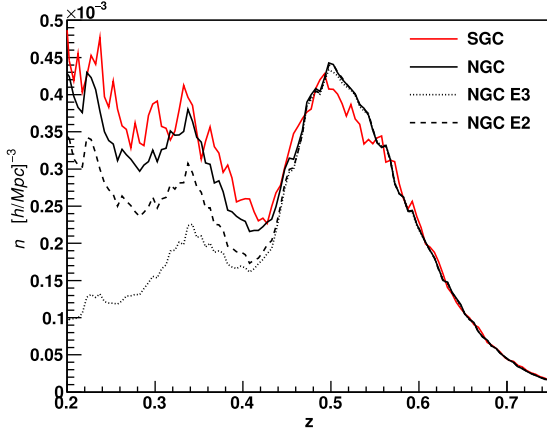
Figure 1. Galaxy density distribution for the North Galactic Cap (NGC, red), South Galactic Cap (SGC, black) as well as the early (E) regions 2 and 3, consisting of chunks 2–6 (for details see Section 2).

and Saito et al. (2016) using the deeper galaxy sample of S82-MGC (Bundy et al. 2015).

The DR12 data release also includes a few regions on the sky (early regions, chunks 2–6), which have not been included in previous data releases. Galaxies in these regions were selected with different algorithms from those of subsequent data. We now create separate masks for chunk 2 (LOWZE2) and chunks 3–6 (LOWZE3) and combine these regions with the rest of the BOSS data set. However, the density for chunks 2–6 is generally lower compared to the rest of the data set, as shown in Fig. 1. Since chunks 2–6 are located in the NGC, the expected bias parameters are different for NGC and SGC. We will address this issue further in Section 5.3. Details about the selection differences between chunks 2–6 and the rest of the BOSS data set as well as the mask creation can be found in Reid et al. (2016).

We include three different incompleteness weights to account for shortcomings of the BOSS data set (see Ross et al. 2012 and Anderson et al. 2014 for details): a redshift failure weight, $w_{\rm rf}$, a fibre collision weight, $w_{\rm fc}$, and a systematics weight, $w_{\rm sys}$, which is a combination of a stellar density weight and a seeing condition weight. Each galaxy is thus counted as

$$w_{\rm c} = (w_{\rm rf} + w_{\rm fc} - 1)w_{\rm sys}. \tag{1}$$

Accounting for redshift failure and fibre collisions, the weighted galaxy count is 1 265 350 (see Table 1).

We divide the BOSS data set into three overlapping redshift bins defined by $0.2 < z < 0.5$, $0.4 < z < 0.6$ and $0.5 < z < 0.75$. The effective redshift for these samples can be calculated as

$$z_{\rm eff} = \frac{\sum_i^{N_{\rm gal}} w_{\rm FKP}(\boldsymbol{x}_i)w_{\rm c}(\boldsymbol{x}_i)z_i}{\sum_i^{N_{\rm gal}} w_{\rm FKP}(\boldsymbol{x}_i)w_{\rm c}(\boldsymbol{x}_i)}, \tag{2}$$

where $w_{\rm FKP} = 1/(1 + n(z)P_0)$ is a signal-to-noise ratio weight suggested by Feldman, Kaiser & Peacock (1993, we adopt $P_0 = 10\,000\,h^{-3}\,{\rm Mpc}^3$). With the above definition of the effective redshift we find $z_{\rm eff} = 0.38$, 0.51 and 0.61 for the three redshift bins.

3 THE POWER-SPECTRUM ESTIMATOR

We employ the FFT-based anisotropic power-spectrum estimator suggested by Bianchi et al. (2015) and Scoccimarro (2015). This estimator follows the ideas of Feldman et al. (1993), but also al-

lows one to estimate the higher order multipoles by decomposing the power-spectrum estimate into its spatial vector components and performing a series of FFTs for each component. This approach accounts for the different line-of-sights for different galaxy pairs within the local plane-parallel approximation.[1] By using FFTs rather than summing over all galaxy pairs (Yamamoto et al. 2006; Beutler et al. 2014a), this estimator allows a computational complexity of $\mathcal{O}(N \log N)$, which is much faster than a naive pair counting analysis (here, N is the number of grid cells used to bin the data).

The power-spectrum multipoles can be calculated as (Feldman et al. 1993; Yamamoto et al. 2006; Bianchi et al. 2015; Scoccimarro 2015) follows:

$$P_0(\boldsymbol{k}) = \frac{1}{2A}\left[F_0(\boldsymbol{k})F_0^*(\boldsymbol{k}) - S\right], \tag{3}$$

$$P_2(\boldsymbol{k}) = \frac{5}{4A}F_0(\boldsymbol{k})\left[3F_2^*(\boldsymbol{k}) - F_0^*(\boldsymbol{k})\right], \tag{4}$$

$$P_4(\boldsymbol{k}) = \frac{9}{16A}F_0(\boldsymbol{k})\left[35F_4^*(\boldsymbol{k}) - 30F_2^*(\boldsymbol{k}) + 3F_0^*(\boldsymbol{k})\right], \tag{5}$$

with

$$F_0(\boldsymbol{k}) = A_0(\boldsymbol{k}), \tag{6}$$

$$F_2(\boldsymbol{k}) = \frac{1}{k^2}\left[k_x^2 B_{xx} + k_y^2 B_{yy} + k_z^2 B_{zz} \right. \\ \left. + 2\left(k_z k_y B_{xy} + k_x k_z B_{xz} + k_y k_z B_{yz}\right)\right], \tag{7}$$

$$\begin{aligned} F_4(\boldsymbol{k}) = \frac{1}{k^4}\Big[& k_x^4 C_{xxx} + k_y^4 C_{yyy} + k_z^4 C_{zzz} \\ & + 4\left(k_x^3 k_y C_{xxy} + k_x^3 k_z C_{xxz} + k_y^3 k_x C_{yyx}\right. \\ & \left. + k_y^3 k_z C_{yyz} + k_z^3 k_x C_{zzx} + k_z^3 k_y C_{zzy}\right) \\ & + 6\left(k_x^2 k_y^2 C_{xyy} + k_x^2 k_z^2 C_{xzz} + k_y^2 k_z^2 C_{yzz}\right) \\ & + 12 k_x k_y k_z \left(k_x C_{xyz} + k_y C_{yxz} + k_z C_{zxy}\right)\Big] \end{aligned} \tag{8}$$

and

$$A_0(\boldsymbol{k}) = \int {\rm d}\boldsymbol{r}\, F(\boldsymbol{r})e^{i\boldsymbol{k}\cdot\boldsymbol{r}}, \tag{9}$$

$$B_{xy}(\boldsymbol{k}) = \int {\rm d}\boldsymbol{r}\, \frac{r_x r_y}{r^2} F(\boldsymbol{r})e^{i\boldsymbol{k}\cdot\boldsymbol{r}}, \tag{10}$$

$$C_{xyz}(\boldsymbol{k}) = \int {\rm d}\boldsymbol{r}\, \frac{r_x^2 r_y r_z}{r^4} F(\boldsymbol{r})e^{i\boldsymbol{k}\cdot\boldsymbol{r}}. \tag{11}$$

$F(\boldsymbol{r})$ is the overdensity field calculated from the data and random galaxies as

$$F(\boldsymbol{r}) = G(\boldsymbol{r}) - \alpha' R(\boldsymbol{r}), \tag{12}$$

where $\boldsymbol{r}$ is defined on a 3D Cartesian grid, in which we bin all data and random galaxies. The function $G(\boldsymbol{r})$ gives the number of weighted galaxies at the location $\boldsymbol{r}$, while $R(\boldsymbol{r})$ is the equivalent function for the random galaxies. The normalization of the random field is given by $\alpha' = N'_{\rm ran}/N'_{\rm gal}$; $N'_{\rm ran}$ and $N'_{\rm gal}$ are the number of

---

[1] We define the local plane-parallel approximation to be the assumption that the position vectors of a given galaxy pair can be treated as parallel such that $\boldsymbol{x}_h = \frac{\boldsymbol{x}_1 + \boldsymbol{x}_2}{2} \approx \boldsymbol{x}_1 \approx \boldsymbol{x}_2$, while the lines of sight vary for different pairs. The global plane-parallel approximation assumes that the line of sight is fixed for all galaxy pairs. See Beutler et al. (2014a, section 3.1) for more details.

Table 1. The number of galaxies $N_{\rm gal}$, the weighted (incompleteness weight) number of galaxies $N'_{\rm gal}$ and the effective volume for the three redshift bins used in this analysis. Equation (2) produces the effective redshifts of $z_{\rm eff} = 0.38$, 0.51 and 0.61 for the three redshift bins, respectively.

| | $0.2 < z < 0.5$ | | $0.4 < z < 0.6$ | | $0.5 < z < 0.75$ | |
	NGC	SGC	NGC	SGC	NGC	SGC
$N_{\rm gal}$	429 182	174 820	500 875	185 500	435 742	158 262
$N'_{\rm gal}$	445 261	182 678	534 725	197 084	467 504	169 907
$V_{\rm eff}[{\rm Gpc}^3]$	2.7	1.0	3.1	1.1	3.0	1.1

weighted random and data galaxies, respectively. All the integrals above can be solved with FFTs. The normalization is given by

$$A = \alpha' \sum_i^{N_{\rm ran}} n'_{\rm g}(\boldsymbol{x}_i) w^2_{\rm FKP}(\boldsymbol{x}_i), \tag{13}$$

where $n'_{\rm g}$ is the weighted galaxy number density. The shot-noise term is only relevant for the monopole and is given by

$$S = \sum_i^{N_{\rm gal}} \Big[f_{\rm c} w_{\rm c}(\boldsymbol{x}_i) w_{\rm sys}(\boldsymbol{x}_i) w^2_{\rm FKP}(\boldsymbol{x}_i) \tag{14}$$

$$+ (1 - f_{\rm c}) w^2_{\rm c}(\boldsymbol{x}_i) w^2_{\rm FKP}(\boldsymbol{x}_i) \Big] \tag{15}$$

$$+ \alpha'^2 \sum_i^{N_{\rm ran}} w^2_{\rm FKP}(\boldsymbol{x}_i), \tag{16}$$

where $f_{\rm c}$ is the probability of a fibre collided galaxy being associated with its nearest neighbour, which we set to 0.5 based on the study by Guo, Zehavi & Zheng (2012). Guo et al. (2012), however, studied the fibre collision only for the CMASS sample and their fibre collision correction assumes a uniform tiling algorithm. Although this definition of the shot noise deviates from the one used in Beutler et al. (2014a), the difference does not actually impact our analysis since we marginalize over any residual shot-noise component (see Section 5).

The final power spectrum is calculated as the average over spherical k-space shells:

$$P_\ell(k) = \langle P_\ell(\boldsymbol{k}) \rangle = \frac{1}{N_{\rm modes}} \sum_{k - \frac{\Delta k}{2} < |\boldsymbol{k}| < k + \frac{\Delta k}{2}} P_\ell(\boldsymbol{k}), \tag{17}$$

where $N_{\rm modes}$ is the number of $\boldsymbol{k}$ modes in that shell. In our analysis, we use $\Delta k = 0.01\,h\,{\rm Mpc}^{-1}$. We employ a Triangular Shaped Cloud method to assign galaxies to the 3D Cartesian grid and correct for the aliasing effect following Jing (2005). The grid configuration implies a Nyquist frequency of $k_{\rm Ny} = 0.6\,h\,{\rm Mpc}^{-1}$, four times as large as the largest scale used in our analysis ($k_{\rm max} = 0.15\,h^{-1}\,{\rm Mpc}$), and the expected error on the power-spectrum monopole at $k = 0.15\,h^{-1}\,{\rm Mpc}$ due to aliasing is <0.001 per cent (Sefusatti et al. 2016).

4 THE SURVEY WINDOW FUNCTION

In this paper, we include the window-function effect in the power-spectrum model rather than attempting to remove the effect from the data. Unlike Beutler et al. (2014a), our window-function treatment follows the method suggested by Wilson et al. (2015). However, Wilson et al. (2015) employ the global plane-parallel approximation in their derivation by setting $\mu = \hat{k} \cdot \hat{\boldsymbol{\eta}}$, where $\boldsymbol{\eta}$ defines a fixed global line-of-sight vector. The global plane-parallel approximation

might be an acceptable approximation for small angle surveys,[2] but is generally not valid for wide area surveys such as BOSS. In Appendix A, we will rederive this window-function treatment within the local plane-parallel approximation, which justifies its use in our analysis.

The three main steps to include the effect of the window function in our power-spectrum model are as follows.

(i) For each model power spectrum, which we intend to compare to the data, we first calculate the model power-spectrum multipoles and Fourier transform them to determine the correlation function multipoles $\xi_\ell^{\rm model}(s)$.

(ii) We calculate the 'convolved' correlation function $\hat{\xi}_\ell^{\rm model}(s)$ by multiplying the correlation function with the window function.

(iii) We Fourier transform the convolved correlation function multipoles back into Fourier space to get the convolved power-spectrum multipoles, $\hat{P}_\ell(k)$.

The convolved power-spectrum multipoles are given by

$$\hat{P}_\ell(k) = 4\pi(-i)^\ell \int {\rm d}s\, s^2 \hat{\xi}_\ell(s) j_\ell(sk). \tag{18}$$

For our analysis, we need to calculate the convolved monopole, quadrupole and hexadecapole power spectra. The convolved correlation function multipoles in equation (18), relevant for our analysis, are

$$\hat{\xi}_0(s) = \xi_0 W_0^2 + \frac{1}{5} \xi_2 W_2^2 + \frac{1}{9} \xi_4 W_4^2 + \cdots \tag{19}$$

$$\begin{aligned}\hat{\xi}_2(s) = {} & \xi_0 W_2^2 + \xi_2 \left[W_0^2 + \frac{2}{7} W_2^2 + \frac{2}{7} W_4^2 \right] \\ & + \xi_4 \left[\frac{2}{7} W_2^2 + \frac{100}{693} W_4^2 + \frac{25}{143} W_6^2 \right] \\ & + \cdots \end{aligned} \tag{20}$$

$$\begin{aligned}\hat{\xi}_4(s) = {} & \xi_0 W_4^2 + \xi_2 \left[\frac{18}{35} W_2^2 + \frac{20}{77} W_4^2 + \frac{45}{143} W_6^2 \right] \\ & + \xi_4 \left[W_0^2 + \frac{20}{77} W_2^2 + \frac{162}{1001} W_4^2 \right. \\ & \left. + \frac{20}{143} W_6^2 + \frac{490}{2431} W_8^2 \right] \\ & + \cdots \end{aligned} \tag{21}$$

We truncate after the hexadecapole contribution of the correlation function but use all window-function multipoles up to $\ell = 8$.

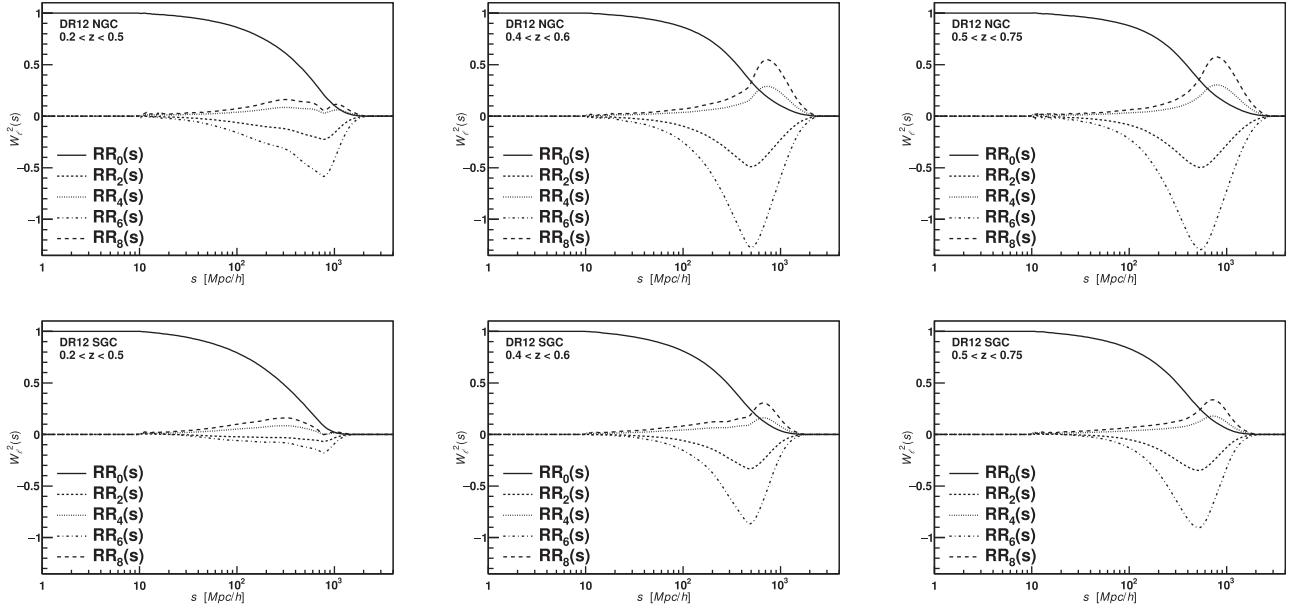[2] Wilson et al. (2015) apply their formalism to the VIPERS survey (Garilli et al. 2014).

Figure 2. Window-function multipoles for BOSS DR12 as given in equation (22) and used for the convolved correlation functions in equations (19)–(21). The top panels display the window functions for the NGC in the three redshift bins used in this analysis; the bottom panels show the window functions for the SGC.

The different window-function multipoles included in our analysis can be derived from the random pair distribution as

$$W_\ell^2(s) \propto \sum_{x_1} \sum_{x_2} RR(s, \mu_s) \mathcal{L}_\ell(\mu_s). \tag{22}$$

The first five non-zero window functions used in our analysis are shown in Fig. 2. The shape of these functions can be understood by investigating equation (22). The monopole is a spherically averaged function, and on small scales, where survey edge effects do not matter, the window will be equal to 1 (given the choice of our normalization). Similarly, the quadrupole, which is an integral over a function oscillating around zero, will average to zero on small scales, while as soon as it reaches scales as large as the survey, it will no longer average to zero.

Fig. 3 shows the unconvolved and convolved power-spectrum multipoles for the SGC in the lowest redshift bin. Given that the SGC in the smallest redshift bin has the smallest volume, we expect window-function effects to be largest in this case.

When one reaches the scale of the survey, the window function becomes crucial for the correct interpretation of the data. We find a significant leakage of power from the quadrupole to the monopole on large scales due to the window function. The effect is shown in Fig. 4, which presents the ratio of the convolved power-spectrum monopole relative to the unconvolved (linear) power-spectrum monopole. The window-function effect is of the order of 2 per cent for $k \lesssim 0.04 \, h \, \mathrm{Mpc}^{-1}$ and significantly increases for $k \lesssim 0.01 \, h \, \mathrm{Mpc}^{-1}$. The quadrupole contribution to the monopole becomes significant at $k \lesssim 0.015 \, h \, \mathrm{Mpc}^{-1}$. The hexadecapole contribution (see the difference between the red and the black lines in Fig. 4) is negligible on all scales. While these effects are of minor importance for our analysis given that we have a minimum k value of $0.01 \, h \, \mathrm{Mpc}^{-1}$, they can be quite important for studies of non-Gaussianity, where the observable is at very small k.

We also tested our window-function treatment by comparing the power-spectrum multipoles for 84 CMASS-like mock catalogues with the convolved multipoles of the corresponding periodic boxes (see
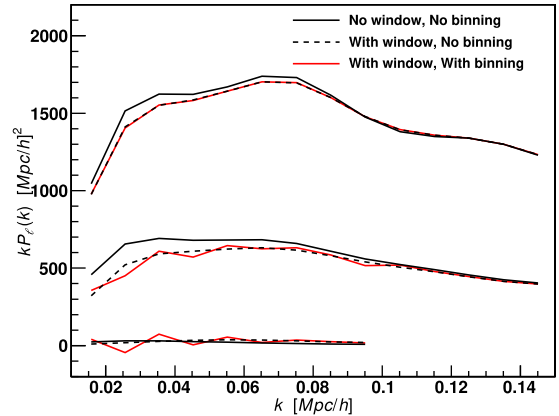

Figure 3. Illustration of the discreteness and the window-function effects on the power-spectrum multipoles for the low-redshift bin in the SGC. The monopole (top), the quadrupole (middle) and hexadecapole (bottom) are displayed in the range used in this analysis. The solid black lines show the input linear power-spectrum multipoles using a linear bias of $b_1 = 2$ and a growth rate of $f = 0.7$, while the black dashed lines are the same power spectra convolved with the window function. The main effect of the window function is a damping at small k. The red line also includes the discreteness effect using equation (40). The discreteness effect is caused by the finite k-space grid, used to estimate the power-spectrum multipoles (see Section 5.1).

Fig. 5). The agreement is far better than the measurement uncertainties and confirms that our convolution method is capturing the geometric effects correctly.

5 THE POWER-SPECTRUM MODEL

Our model for the anisotropic galaxy power spectrum is based on the work of Taruya, Nishimichi & Saito (2010, TNS) and is the same as used in our DR11 analysis (Beutler et al. 2014a). We summarize this model below but refer the reader to Beutler et al. (2014a) for more details.
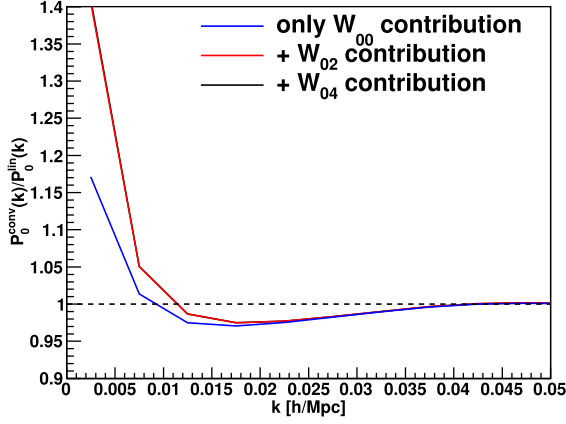
Figure 4. The leakage of higher order multipoles to the observed monopole power spectrum due to the window-function effect. The blue line shows the contribution from the monopole to the observed monopole; the red line indicates the contributions from the monopole and quadrupole and the black line represents the contributions from the monopole, quadrupole and hexadecapole. The total window-function effect (black) is of the order of 2 per cent for $k \lesssim 0.04\,h\,\mathrm{Mpc}^{-1}$ and significantly increases for $k \lesssim 0.01\,h\,\mathrm{Mpc}^{-1}$. The quadrupole contribution (from the difference between the blue and red lines) becomes significant at $k \lesssim 0.015\,h\,\mathrm{Mpc}^{-1}$. The hexadecapole contribution (from the difference between the red and the black lines) is negligible on all scales.

The anisotropic power spectrum is given by

$$P_g(k, \mu) = \exp\left\{-(fk\mu\sigma_v)^2\right\}\left[P_{g,\delta\delta}(k)\right.$$
$$\left. + 2f\mu^2 P_{g,\delta\theta}(k) + f^2\mu^4 P_{\theta\theta}(k)\right.$$
$$\left. + b_1^3 A(k, \mu, \beta) + b_1^4 B(k, \mu, \beta)\right], \quad (23)$$

where μ denotes the cosine of the angle between the wavenumber vector and the line-of-sight direction. The overall exponential factor represents the suppression due to the 'Finger of God' (FoG) effect, and we treat σ_v as a free parameter.

The first three terms in the square brackets in equation (23) describe an extension to the simple Kaiser model. The density ($P_{\delta\delta}$), velocity divergence ($P_{\theta\theta}$) and their cross-power spectra ($P_{\delta\theta}$) are identical in linear theory, while in the quasi non-linear regime, the density power spectrum increases and velocities are randomized on small scales, which damp the velocity power spectrum (Scoccimarro 2004). In addition to this fact, we need to relate the density and velocity fields for (dark) matter to those of galaxies. Here we assume no velocity bias, i.e. $\theta_g = \theta$, but include every possible galaxy bias term at the next-to-leading order using symmetry arguments (McDonald & Roy 2009):

$$P_{g,\delta\delta}(k) = b_1^2 P_{\delta\delta}(k) + 2b_2 b_1 P_{b2,\delta}(k) + 2b_{s2} b_1 P_{bs2,\delta}(k)$$
$$+ 2b_{3nl} b_1 \sigma_3^2(k) P_m^{\mathrm{lin}}(k) + b_2^2 P_{b22}(k)$$
$$+ 2b_2 b_{s2} P_{b2s2}(k) + b_{s2}^2 P_{bs22}(k) + N, \quad (24)$$

$$P_{g,\delta\theta}(k) = b_1 P_{\delta\theta}(k) + b_2 P_{b2,\theta}(k) + b_{s2} P_{bs2,\theta}(k)$$
$$+ b_{3nl} \sigma_3^2(k) P_m^{\mathrm{lin}}(k), \quad (25)$$

where P_m^{lin} is the linear matter power spectrum. Here, we introduce five galaxy bias parameters: the renormalized linear bias, b_1, second-order local bias, b_2, second-order non-local bias, b_{s2}, third-order non-local bias, b_{3nl}, and the constant stochasticity term, N. We evaluate the non-linear matter power spectra, $P_{\delta\delta}$, $P_{\delta\theta}$, $P_{\theta\theta}$, with

the RegPT scheme at two-loop order (Taruya et al. 2012) using the fiducial cosmology specified at the end of Section 1. The other bias terms are given by

$$P_{b2,\delta}(k) = \int \frac{\mathrm{d}^3 q}{(2\pi)^3} P_m^{\mathrm{lin}}(q) P_m^{\mathrm{lin}}(|\mathbf{k} - \mathbf{q}|) F_S^{(2)}(\mathbf{q}, \mathbf{k} - \mathbf{q}), \quad (26)$$

$$P_{b2,\theta}(k) = \int \frac{\mathrm{d}^3 q}{(2\pi)^3} P_m^{\mathrm{lin}}(q) P_m^{\mathrm{lin}}(|\mathbf{k} - \mathbf{q}|) G_S^{(2)}(\mathbf{q}, \mathbf{k} - \mathbf{q}), \quad (27)$$

$$P_{bs2,\delta}(k) = \int \frac{\mathrm{d}^3 q}{(2\pi)^3} P_m^{\mathrm{lin}}(q) P_m^{\mathrm{lin}}(|\mathbf{k} - \mathbf{q}|)$$
$$\times F_S^{(2)}(\mathbf{q}, \mathbf{k} - \mathbf{q}) S^{(2)}(\mathbf{q}, \mathbf{k} - \mathbf{q}), \quad (28)$$

$$P_{bs2,\theta}(k) = \int \frac{\mathrm{d}^3 q}{(2\pi)^3} P_m^{\mathrm{lin}}(q) P_m^{\mathrm{lin}}(|\mathbf{k} - \mathbf{q}|)$$
$$\times G_S^{(2)}(\mathbf{q}, \mathbf{k} - \mathbf{q}) S^{(2)}(\mathbf{q}, \mathbf{k} - \mathbf{q}), \quad (29)$$

$$P_{b22}(k) = \frac{1}{2} \int \frac{\mathrm{d}^3 q}{(2\pi)^3} P_m^{\mathrm{lin}}(q) \left[P_m^{\mathrm{lin}}(|\mathbf{k} - \mathbf{q}|) - P_m^{\mathrm{lin}}(q) \right], \quad (30)$$

$$P_{b2s2}(k) = -\frac{1}{2} \int \frac{\mathrm{d}^3 q}{(2\pi)^3} P_m^{\mathrm{lin}}(q) \left[\frac{2}{3} P_m^{\mathrm{lin}}(q) \right.$$
$$\left. - P_m^{\mathrm{lin}}(|\mathbf{k} - \mathbf{q}|) S^{(2)}(\mathbf{q}, \mathbf{k} - \mathbf{q}) \right], \quad (31)$$

$$P_{bs22}(k) = -\frac{1}{2} \int \frac{\mathrm{d}^3 q}{(2\pi)^3} P_m^{\mathrm{lin}}(q) \left[\frac{4}{9} P_m^{\mathrm{lin}}(q) \right.$$
$$\left. - P_m^{\mathrm{lin}}(|\mathbf{k} - \mathbf{q}|) S^{(2)}(\mathbf{q}, \mathbf{k} - \mathbf{q})^2 \right], \quad (32)$$

where the symmetrized second-order PT kernels, $F_S^{(2)}$, $G_S^{(2)}$ and $S^{(2)}$ are given by

$$F_S^{(2)}(\mathbf{q}_1, \mathbf{q}_2) = \frac{5}{7} + \frac{\mathbf{q}_1 \cdot \mathbf{q}_2}{2q_1 q_2}\left(\frac{q_1}{q_2} + \frac{q_2}{q_1}\right) + \frac{2}{7}\left(\frac{\mathbf{q}_1 \cdot \mathbf{q}_2}{q_1 q_2}\right)^2, \quad (33)$$

$$G_S^{(2)}(\mathbf{q}_1, \mathbf{q}_2) = \frac{3}{7} + \frac{\mathbf{q}_1 \cdot \mathbf{q}_2}{2q_1 q_2}\left(\frac{q_1}{q_2} + \frac{q_2}{q_1}\right) + \frac{4}{7}\left(\frac{\mathbf{q}_1 \cdot \mathbf{q}_2}{q_1 q_2}\right)^2, \quad (34)$$

$$S^{(2)}(\mathbf{q}_1, \mathbf{q}_2) = \left(\frac{\mathbf{q}_1 \cdot \mathbf{q}_2}{q_1 q_2}\right)^2 - \frac{1}{3}. \quad (35)$$

If we additionally define

$$D^{(2)}(\mathbf{q}_1, \mathbf{q}_2) = \frac{2}{7}\left[S^{(2)}(\mathbf{q}_1, \mathbf{q}_2) - \frac{2}{3}\right], \quad (36)$$

we can express $\sigma_3^2(k)$ of equation (25) as

$$\sigma_3^2(k) = \frac{105}{16} \int \frac{\mathrm{d}^3 q}{(2\pi)^3} P_m^{\mathrm{lin}}(q) \left[D^{(2)}(-\mathbf{q}, \mathbf{k}) S^{(2)}(\mathbf{q}, \mathbf{k} - \mathbf{q}) + \frac{8}{63} \right]. \quad (37)$$

In the case of the local Lagrangian bias picture, we can predict the amplitude of the non-local bias as (Saito et al. 2014)

$$b_{s2} = -\frac{4}{7}(b_1 - 1), \quad (38)$$

$$b_{3nl} = \frac{32}{315}(b_1 - 1), \quad (39)$$

which are in good agreement with N-body simulations (e.g. Baldauf et al. 2012). The impact of second-order tidal bias on the power spectrum is expected to be very small on the scales included in this analysis, while the impact of the third-order non-local bias is expected to be larger than the second-order contribution, as shown

in Saito et al. (2014). Nevertheless, we argue that our assumption does not have an impact for our purpose, since we validate our modelling well within the precision of the final constraints in the test with the mock challenge.

In this work, we adopt these relations for simplicity, while we take b_1, b_2 and N as independent parameters to vary. Since we measure the amplitude of the biased clustering, the actual free parameters used are $b_1\sigma_8(z)$, $b_2\sigma_8(z)$ and N at each redshift bin, as discussed in Section 5.3.

Our RSD model is based on the local distant observer approximation, i.e. without accounting for the wide angle effect. The wide angle effect has been shown to be negligible compared to the sample variance for surveys such as BOSS (Beutler et al. 2011, 2012; Samushia, Percival & Raccanelli 2011; Yoo & Seljak 2015).

Recently, potential improvements for the model discussed above have been proposed. For the non-linear RSD model, Zheng & Song (2016) try to improve the TNS model by further examining our FoG suppression term and directly comparing the correction terms between perturbation theory and simulations. For the non-linear galaxy bias, Lazeyras et al. (2016) study the separate universe simulations that enable to directly measure and assess the non-linear local bias of dark matter haloes (see also Li, Hu & Takada 2016). They also discuss the importance of the k^2 bias term that we ignore just for simplicity (see also McDonald & Roy 2009; Biagetti et al. 2014; Schmidt 2016 etc.). Also, the developments in terms of the distribution function approach (e.g. Okumura et al. 2015) and the effective field theory approach (e.g., Lewandowski et al. 2015) are ongoing and can be complementary to our model.

5.1 Correction for the irregular μ distribution

Because the survey volume is not infinite, the measured power spectra are estimated on a finite and discrete k-space grid. Performing FFTs in a Cartesian lattice makes the angular distribution of the Fourier modes irregular and causes increasing deviation from the isotropic distribution at smaller k. As a result, fluctuation-like deviations appear in the measured power-spectrum multipoles that are not caught by the window function, as shown in the bottom panel (SGC) of Fig. 6. The effect is larger for the quadrupole than the monopole since the quadrupole is more sensitive to an anisotropy. Our DR11 analysis corrected the measured data for this effect, while here we include this effect in our power-spectrum model. When integrating the model power spectrum $P(k, \mu)\mathcal{L}(\mu)$ in equation (40) over μ, we weight each μ bin by the normalized number of modes $N(k, \mu)$ counted on the k-space grid used to estimate the power spectrum.

$$P_\ell(k) = \int_{-1}^{1} \mathrm{d}\mu \; P(k, \mu) \frac{N_{\mathrm{modes}}(k, \mu)}{N_{\mathrm{bin}}(k)} \mathcal{L}_\ell(\mu), \tag{40}$$

with the normalization for each k given by

$$N_{\mathrm{bin}}(k) = \int_{-1}^{1} \mathrm{d}\mu \; N_{\mathrm{modes}}(k, \mu). \tag{41}$$

This $P_\ell(k)$ is used to calculate ξ_ℓ in equations (19)–(21). Fig. 3 shows the effect of irregular μ distribution in the three power-spectrum multipoles. While the effect is most pronounced in the higher order multipoles, it never exceeds the measurement uncertainties and hence is not a dominant effect.

The inclusion of a μ-dependent function in equation (40) is inconsistent with our derivation of the window-function convolution in equation (A12). A completely consistent approach would include the effect of irregular μ distribution after the window-function convolution, or would properly include this function in equation (A12).
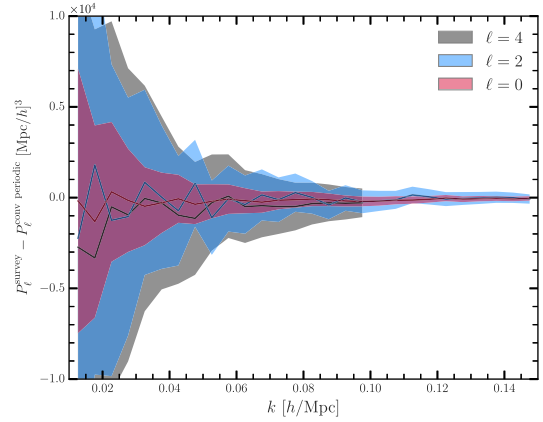

Figure 5. Here we show the difference between the mean power-spectrum multipoles of a set of cMASS-like mock catalogues and the mean power-spectrum multipoles of the corresponding periodic boxes convolved with the window function. A value of zero indicates that our window-function convolution method does correctly model the effects introduced by the survey geometry. The colour bands indicate the uncertainties as given by the diagonal terms of the NGC covariance matrix for the second redshift bin.

We tested the impact of this assumption by including the discreteness effect after the convolution (using multipole expansion) and found that this does not change our results.

5.2 The Alcock–Paczynski effect

When transforming our observables, such as celestial position and redshift, into physical coordinates, we assume specific relations between the redshift and the line-of-sight distance (i.e. the Hubble parameter) and between the angular separation and the distance perpendicular to the line of sight (i.e. the angular diameter distance) given by the fiducial cosmological model. Therefore, if we assume a fiducial cosmology that is different from the true cosmology, it will produce geometric warping and artificially introduce an anisotropy in an otherwise isotropic feature in the galaxy clustering, independently from the effect of RSD. This behaviour is known as the AP effect (Alcock & Paczynski 1979) and can be used to measure cosmological parameters (Ballinger et al. 1996; Matsubara & Suto 1996). The anisotropy due to the AP effect is often difficult to separate from the RSD effect for a featureless power spectrum given the uncertainties in the models for RSD (Seo & Eisenstein 2003; Shoji, Jeong & Komatsu 2009). The presence of the BAO feature in the power spectrum, however, helps to break this degeneracy.

To account for the AP effect due to the different geometric scaling along and perpendicular to the line-of-sight directions between the true and fiducial cosmology, we introduce the scaling factors

$$\alpha_\parallel = \frac{H^{\mathrm{fid}}(z)r_{\mathrm{s}}^{\mathrm{fid}}(z_{\mathrm{d}})}{H(z)r_{\mathrm{s}}(z_{\mathrm{d}})}, \tag{42}$$

$$\alpha_\perp = \frac{D_{\mathrm{A}}(z)r_{\mathrm{s}}^{\mathrm{fid}}(z_{\mathrm{d}})}{D_{\mathrm{A}}^{\mathrm{fid}}(z)r_{\mathrm{s}}(z_{\mathrm{d}})}, \tag{43}$$

where $H^{\mathrm{fid}}(z)$ and $D_{\mathrm{A}}^{\mathrm{fid}}(z)$ are the fiducial values for the Hubble parameter and angular diameter distance at the effective redshifts of the data set, and $r_{\mathrm{s}}^{\mathrm{fid}}(z_{\mathrm{d}})$ is the fiducial value of the sound horizon scale at the drag epoch assumed in the power-spectrum template. By using the sound horizon scale as the reference scale for the AP test, we are assuming that the main feature that contributes to the AP test is the BAO. The true wavenumbers $k'_\parallel$ and $k'_\perp$ are then related to the observed wavenumbers by $k'_\parallel = k_\parallel/\alpha_\parallel$ and $k'_\perp = $
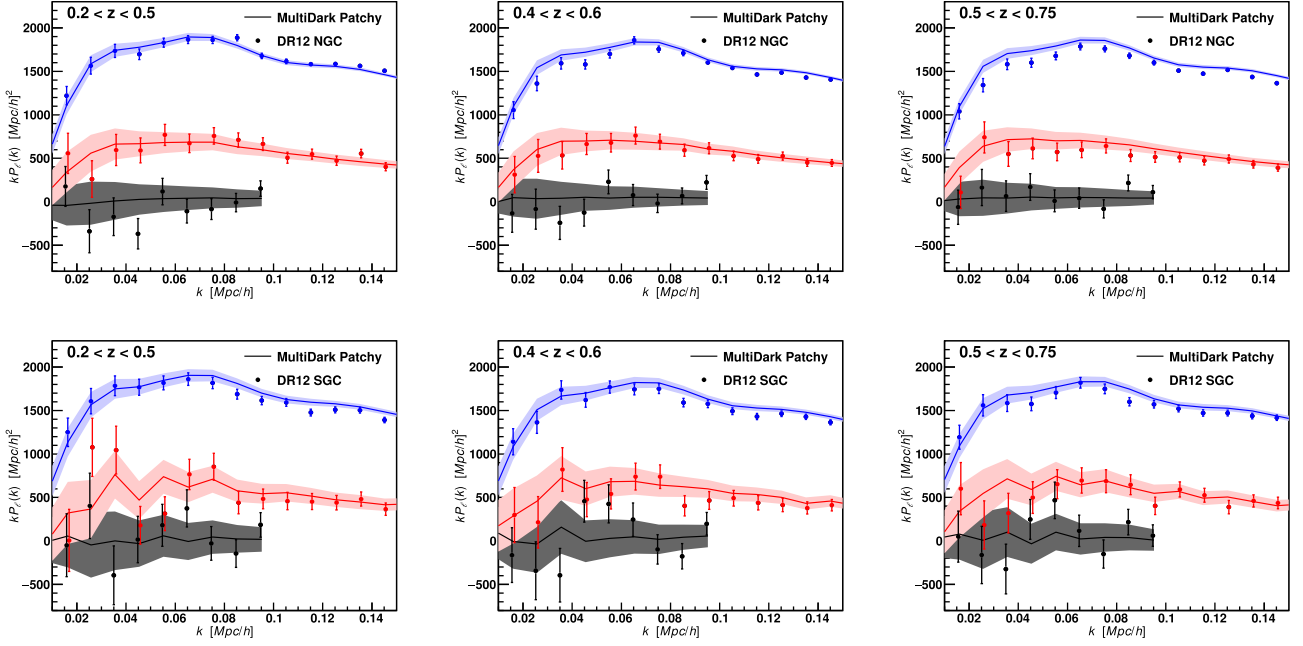
Figure 6. Comparison of the BOSS DR12 power-spectrum multipoles (coloured data points) and the mean of the MultiDark-PATCHY mock catalogues (coloured solid lines) with the same selection function as the data. The top panels show the power-spectrum multipoles for the three redshift bins in the NGC and the bottom panels are the same measurements for SGC. The different multipoles are colour coded, where blue represents the monopole, red represents the quadrupole and black shows the hexadecapole. The shaded area is the variance between all mock catalogues and is identical to the extent of the error bars on the data points. For SGC (bottom panels), the mock catalogues show some correlated fluctuations at small k, which is most prominent in the higher order multipoles. This feature is a discreteness effect, due to the finite number of modes at large scales. This effect is present in the data as well, and we discuss how to account for this effect in our power-spectrum model in Section 5.1.

$k_\perp/\alpha_\perp$. Transferring this information into scalings for the absolute wavenumber $k = \sqrt{k_\parallel^2 + k_\perp^2}$ and the cosine of the angle to the line-of-sight μ, we can relate the true (k', μ') and observed values (k, μ) by (Ballinger et al. 1996)

$$k' = \frac{k}{\alpha_\perp} \left[1 + \mu^2 \left(\frac{1}{F^2} - 1 \right) \right]^{1/2}, \tag{44}$$

$$\mu' = \frac{\mu}{F} \left[1 + \mu^2 \left(\frac{1}{F^2} - 1 \right) \right]^{-1/2}, \tag{45}$$

with $F = \alpha_\parallel/\alpha_\perp$. The multipole power spectrum including the AP effect can then be written as

$$P_\ell(k) = \left(\frac{r_s^{\rm fid}}{r_s} \right)^3 \frac{(2\ell + 1)}{2\alpha_\perp^2 \alpha_\parallel} \int_{-1}^{1} d\mu \, P_g \left[k'(k, \mu), \mu'(\mu) \right] \mathcal{L}_\ell(\mu), \tag{46}$$

where we use the model of Section 5 for $P_g[k'(k, \mu), \mu'(\mu)]$. The factor $(\frac{r_s^{\rm fid}}{r_s})^3 \frac{1}{2\alpha_\perp^2 \alpha_\parallel}$ accounts for the difference in the cosmic volume in different cosmologies. The ratio of sound horizon scales is needed to compensate for the sound horizon scale included in the definitions of the α values. To treat this r_s properly, we could apply the *Planck* measurement (Planck Collaboration XIII 2016) on r_s as a prior during the parameter fitting. Since the *Planck* uncertainty on r_s is only at the level of $\sim$0.2 per cent, fixing $r_s = 147.41 \, h^{-1}$ Mpc has a negligible effect on our measurements of $\alpha_\parallel$ and $\alpha_\perp$.

The AP effect (from the anisotropic warping of the BAO) constrains the parameter combination $F_{\rm AP}(z) = (1 + z)D_A(z)H(z)/c$, while the radial dilation of the BAO feature constrains the combination $D_V(z)/r_s(z_d) \propto \left[D_A^2(z)/H(z) \right]^{1/3}$. Together these two signals allow one to break the degeneracy between $D_A(z)$ and $H(z)$.

5.3 Model parametrization

Based on the discussion of our model in Section 5 we have four nuisance parameters, $b_1\sigma_8$, $b_2\sigma_8$, σ_v and N, which we fit to our measurements together with the three cosmological parameters $f\sigma_8$, $\alpha_\parallel$ and $\alpha_\perp$. We need to put a prior on σ_8 when calculating the higher order corrections, where we use the fiducial value of $\sigma_8 = 0.8$. Note that this prior only affects the second-order correction, while the linear contribution in the form of $b_1\sigma_8$ is a free parameter. The two α parameters carry the BAO and AP information; we can rephrase these parameters to

$$F_{\rm AP} = (1 + z_{\rm eff})D_A(z_{\rm eff})H(z_{\rm eff})/c \tag{47}$$

$$= \frac{\alpha_\perp}{\alpha_\parallel}(1 + z_{\rm eff})D_A^{\rm fid}(z_{\rm eff})H^{\rm fid}(z_{\rm eff})/c \tag{48}$$

and

$$D_V(z_{\rm eff})\frac{r_s^{\rm fid}(z_d)}{r_s(z_d)} = \left(\alpha_\perp^2 \alpha_\parallel [(1 + z_{\rm eff})D_A^{\rm fid}(z_{\rm eff})]^2 \frac{cz_{\rm eff}}{H^{\rm fid}(z_{\rm eff})} \right)^{\frac{1}{3}}. \tag{49}$$

At low redshift the BOSS galaxies follow a slightly different selection in the SGC and NGC (see Section 2, Reid et al. 2016 and Ross et al. 2016). These differences lead to different power-spectrum amplitudes in the SGC and NGC. To account for this issue, we marginalize over the four nuisance parameters independently for NGC and SGC, while we use the same cosmological parameters. Tests on mock catalogues demonstrated that using separate nuisance parameters for the NGC and SGC does not degrade our cosmological constraints. We therefore have a total of 11 parameters for each redshift bin in our analysis: $b_1^{\rm NGC}\sigma_8(z)$, $b_1^{\rm SGC}\sigma_8(z)$, $b_2^{\rm NGC}\sigma_8(z)$, $b_2^{\rm SGC}\sigma_8(z)$, $\sigma_v^{\rm NGC}$, $\sigma_v^{\rm SGC}$, $N^{\rm NGC}$, $N^{\rm SGC}$, $f(z)\sigma_8(z)$, $\alpha_\parallel$ and $\alpha_\perp$.

6 MOCK CATALOGUES

To derive a covariance matrix for the power-spectrum multipoles we use the MultiDark-PATCHY mock catalogues (Kitaura et al. 2016). These mock catalogues have been calibrated to an *N*-body-based reference sample using approximate gravity solvers and analytical–statistical biasing models. The reference catalogue is extracted from one of the BigMultiDark simulations (Klypin et al. 2016), which used 3840^3 particles on a volume of $(2.5\,h^{-1}\,\mathrm{Mpc})^3$ assuming a ΛCDM cosmology with $\Omega_{\rm m} = 0.307115$, $\Omega_{\rm b} = 0.048206$, $\sigma_8 = 0.8288$, $n_{\rm s} = 0.9611$, and a Hubble constant of $H_0 = 67.77\,\mathrm{km\,s^{-1}\,Mpc^{-1}}$.

Halo abundance matching is used to reproduce the observed BOSS two- and three-point clustering measurements (Rodrıguez-Torres et al. 2016). This technique is applied at different redshift bins to reproduce the BOSS DR12 redshift range. These mock catalogues are combined into light cones, also accounting for selection effects and masking. In total, we have 2045 mock catalogues available for the NGC and 2048 mock catalogues for the SGC.

The mean power-spectrum multipoles for MultiDark-PATCHY mock catalogues are shown in Fig. 6 (lines with shaded area) for the NGC (top panels) and SGC (bottom panels), together with the BOSS measurements (coloured points with error bars). The mock catalogues closely reproduce the data power-spectrum multipoles for the entire range of wavenumbers relevant for this analysis.

The SGC mock catalogues show some correlated fluctuations in the power spectra at small *k*, which are more prominent in the quadrupole and hexadecapole. This behaviour is a discreteness effect due to the finite number of Fourier modes, which is more severe at small *k*. This effect is present in the data as well; we discuss how to account for this effect in our power-spectrum model in Section 5.1.

6.1 The covariance matrix

We can derive a covariance matrix from the set of mock catalogues described in the last section as

$$\mathbf{C}_{xy} = \frac{1}{N_{\rm s}-1} \sum_{n=1}^{N_{\rm s}} \left[P_{\ell,n}(k_i) - \overline{P}_\ell(k_i) \right]$$
$$\times \left[P_{\ell',n}(k_j) - \overline{P}_{\ell'}(k_j) \right], \tag{50}$$

with $N_{\rm s}$ being the number of mock catalogues. Our covariance matrix contains the monopole, quadrupole and hexadecapole uncertainties as well as their covariances. The elements of the matrices are given by $(x, y) = (\frac{n_{\rm b}\ell}{2} + i, \frac{n_{\rm b}\ell'}{2} + j)$, where $n_{\rm b}$ is the number of bins in each multipole power spectrum. Our fitting range is $k = 0.01$–$0.15\,h\,\mathrm{Mpc}^{-1}$ for the monopole and quadrupole ($n_{\rm b} = 14$), and $k = 0.01$–$0.10\,h\,\mathrm{Mpc}^{-1}$ for the hexadecapole ($n_{\rm b} = 9$); hence, the dimensions of the covariance matrices are 37×37. The mean of the power spectra is defined as

$$\overline{P}_\ell(k_i) = \frac{1}{N_{\rm s}} \sum_{n=1}^{N_{\rm s}} P_{\ell,n}(k_i). \tag{51}$$

Since the mock catalogues have the same selection function as the data, they automatically incorporate the window-function and integral-constraint effects present in the data.

Fig. 7 presents the correlation matrices for the three redshift bins of BOSS NGC (top panels) and SGC (bottom panels), where the correlation coefficient is defined as

$$r_{xy} = \frac{\mathbf{C}_{xy}}{\sqrt{\mathbf{C}_{xx}\mathbf{C}_{yy}}}. \tag{52}$$

Each panel shows a matrix with three horizontal and vertical division lines. The first column displays the correlation between *k* bins in the monopole with itself (bottom), with the quadrupole (middle) and with the hexadecapole (top). The second column is the correlations for the quadrupole and the third column presents the correlations for the hexadecapole. There is a correlation between the monopole and quadrupole, as well as a correlation between the quadrupole and hexadecapole, while the correlation between the monopole and hexadecapole is quite weak.

Since the estimated covariance matrix $\mathbf{C}$ is inferred from mock catalogues, its inverse, $\mathbf{C}^{-1}$, provides a biased estimate of the true inverse covariance matrix, due to the skewed nature of the inverse Wishart distribution (Hartlap, Simon & Schneider 2007). To correct for this bias, we rescale the inverse covariance matrix as

$$\mathbf{C}^{-1}_{ij,\mathrm{Hartlap}} = \frac{N_{\rm s} - n_{\rm b} - 2}{N_{\rm s} - 1} \mathbf{C}^{-1}_{ij}, \tag{53}$$

where $n_{\rm b}$ is the number of power-spectrum bins. With these covariance matrices, we can perform a standard χ^2 minimization to find the best-fitting parameters. In our analysis, we have $N_{\rm s} = 2048\,(2045)$ and $n_{\rm b} = 37$, which yield a Hartlap factor of ~ 0.98, representing an increase in the variance of about 1 per cent.

6.2 Fitting preparation

Using the covariance matrix derived in Section 6.1, we perform a χ^2 minimization to find the best-fitting parameters. In addition to the scaling of the covariance matrix of equation (53), we have to propagate the error in the covariance matrix to the error on the estimated parameters. This test is accomplished by scaling the variance for each parameter by (Percival et al. 2014)

$$M_1 = \sqrt{\frac{1 + B(n_{\rm b} - n_{\rm p})}{1 + A + B(n_{\rm p} + 1)}}, \tag{54}$$

where $n_{\rm p}$ is the number of parameters, and

$$A = \frac{2}{(N_{\rm s} - n_{\rm b} - 1)(N_{\rm s} - n_{\rm b} - 4)}, \tag{55}$$

$$B = \frac{N_{\rm s} - n_{\rm b} - 2}{(N_{\rm s} - n_{\rm b} - 1)(N_{\rm s} - n_{\rm b} - 4)}. \tag{56}$$

Taking the quantities that apply in our case $[N_{\rm s} = 2048\,(2045)$, $n_{\rm b} = 76, n_{\rm p} = 11]$ results in a modest correction of $M_1 \approx 1.01$.

When dealing with the variance or standard deviation of a distribution of finite mock results that also has been fitted with a covariance matrix derived from the same mock results, the standard deviation from these mocks must be corrected as

$$M_2 = M_1 \sqrt{\frac{N_{\rm s} - 1}{N_{\rm s} - n_{\rm b} - 2}}. \tag{57}$$

When the error is estimated from the likelihood distribution, the resulting standard deviation is multiplied by M_1 alone since the second factor, i.e. Hartlap factor (Hartlap et al. 2007), is already included in equation (53).

We calculate the power spectrum in bins of $\Delta k = 0.01\,h\,\mathrm{Mpc}^{-1}$. Tests on mock data sets have shown that such a binning choice is small enough so that it does not dilute any of the cosmologically relevant information, while sufficiently large so that it keeps the Hartlap et al. (2007) correction factor small.

The fitting range for our analysis is fixed to $k = 0.01$–$0.15\,h\,\mathrm{Mpc}^{-1}$ for the monopole and quadrupole and $k = 0.01$–$0.1\,h\,\mathrm{Mpc}^{-1}$ for the hexadecapole. This choice is based on many
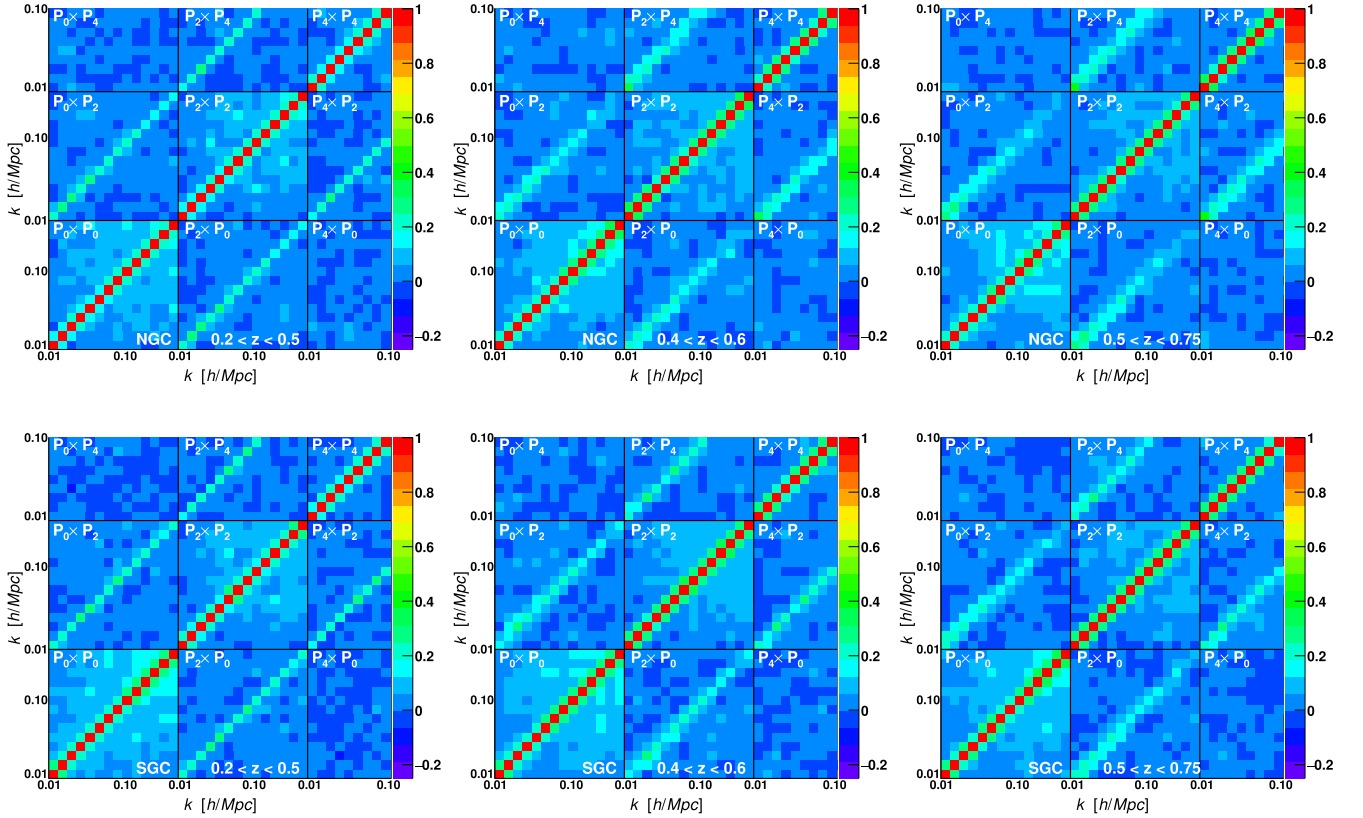
Figure 7. Covariance matrices including the monopole, quadrupole and hexadecapole of the NGC (top) and SGC (bottom) for the three redshift bins used in this analysis. We include all bins between $k = 0.01$ and $0.15\,h^{-1}$ Mpc for the monopole and quadrupole and all bins between $k = 0.01$ and $0.10\,h^{-1}$ Mpc for the hexadecapole. The colour indicates the level of correlation, where red represents 100 per cent correlation and blue–magenta means low level of anticorrelation.

mock tests to get the best-possible unbiased constraints with the available data. Using the hexadecapole up to $k_{\mathrm{max}} = 0.15\,h\,\mathrm{Mpc}^{-1}$ and/or the monopole and quadrupole up to $k_{\mathrm{max}} = 0.2\,h\,\mathrm{Mpc}^{-1}$ does introduce small systematic biases, which we decided to avoid in this analysis.

To derive the likelihood distribution for the different parameters given the measurements we use a Monte Carlo Markov Chain approach based on a modified version of the PYTHON EMCEE package (Foreman-Mackey et al. 2013). We test the convergence of four chains run in parallel using the Gelman & Rubin (1992) convergence criterion.

7 TESTING THE MODEL WITH MOCK CATALOGUES

To confirm that our model is accurate enough to extract the true cosmological parameters within the measurement precision, we refer the reader to our DR11 analysis (Beutler et al. 2014a), where we already performed many tests of our analysis pipeline. Here, we discuss two further investigations: tests on the MD-PATCHY mock catalogues, and the participation on a challenge exercise, conducted on a set of high-fidelity mocks. For the purposes of the results presented in this paper, the latter can be considered a blind test.

7.1 Test using the blind mock challenge results

We participated in a mock challenge within the BOSS galaxy clustering working group (Tinker et al. 2016). This activity was divided into two parts, where (1) we had to reproduce the correct cos-
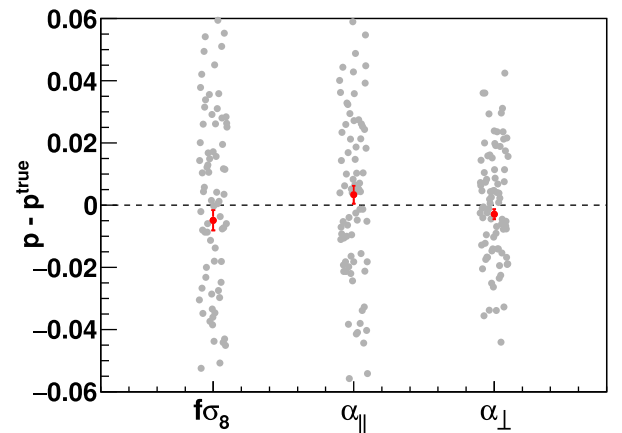

Figure 8. Results of the blind mock challenge for the power-spectrum model used in this analysis when applied to 84 CMASS-like mock catalogues derived from N-body simulations. The grey data points are the results for all 84 mock catalogues for the three parameters of interest. The red data points indicate the mean and error on the mean. The y-axis shows the (absolute) deviation from the true underlying cosmology.

mological parameters for several simulation boxes with different cosmologies and halo occupation distributions set-up, and (2) we were required to reproduce the correct cosmological parameters for a set of 84 N-body-based mock catalogues with the same selection function as the CMASS data set. The results for the second part of the mock challenge are displayed in Fig. 8. Assuming that the

84 mock catalogues are uncorrelated,[3] we can use them to test for potential biases of the model up to the level of $\sqrt{84} = 9.16$ times smaller than the measurement uncertainties. Based on the offsets of our measurements from the true cosmology shown in Fig. 8, we can reproduce the correct cosmological parameters with a bias of $\Delta f\sigma_8 = 0.004\,85$, $\Delta\alpha_\perp = 0.002\,924$ and $\Delta\alpha_\parallel = 0.0034$. These potential biases are $\lesssim 10$ per cent of our measurement uncertainties.

For comparisons of our model to other RSD studies and a more detailed discussion of the blind mock challenge, we refer the reader to Tinker et al. (2016).

7.2 Tests on the MultiDark-PATCHY mock catalogues

We applied our analysis pipeline to the MultiDark-PATCHY mock catalogues; the results are shown in Fig. 9 and Table 2. Fig. 9 presents the maximum-likelihood results for all MultiDark-PATCHY mock catalogues including the hexadecapole (black data points) and excluding the hexadecapole (magenta data points). The red cross indicates the mean and variance between the black data points, while the black dashed lines show the fiducial parameters of the simulation. The results in Table 2 show that including the hexadecapole reduces the scatter by ∼30 per cent, while still reproducing the correct cosmological parameters within 2.7 per cent, 1.3 per cent and 0.5 per cent for $f\sigma_8$, $\alpha_\parallel$ and $\alpha_\perp$.

We can reproduce the fiducial parameters to a similar level as for the mock challenge discussed earlier. However, the MultiDark-PATCHY mock catalogues are not real *N*-body simulations but use approximate methods to allow a large number of mocks to be produced. Therefore, we adopt the blind mock challenge results to determine the potential systematic biases.

8 BOSS DR12 DATA ANALYSIS

Here, we will present the main results of our data analysis. The best-fitting results of the BOSS DR12 data are summarized in Table 3 and plotted in Figs 10–12.

8.1 Cosmological parameter constraints

Marginalizing over all other parameters produces the following constraints on the growth of structure parameter: $f(z_{\text{eff}})\sigma_8(z_{\text{eff}}) = 0.477 \pm 0.051$ at $z_{\text{eff}} = 0.38$, 0.453 ± 0.050 at $z_{\text{eff}} = 0.51$ and 0.410 ± 0.044 at $z_{\text{eff}} = 0.61$ from the low-, middle- and high-redshift bin, respectively. For the AP parameter $F_{\text{AP}} = (1 + z_{\text{eff}})D_{\text{A}}(z_{\text{eff}})H(z_{\text{eff}})/c = 0.424 \pm 0.020$, 0.593 ± 0.031 and 0.732 ± 0.034; for the BAO scale parameter $D_V r_{\text{s}}^{\text{fid}}/r_{\text{s}} = 1490 \pm 33$, 1913 ± 44 and 2134 ± 46 Mpc at $z_{\text{eff}} = 0.38$, 0.51 and 0.61, respectively. These values are our default, final results.

When excluding the hexadecapole, the best-fitting values shift upwards in the high- and middle-redshift bin, while they shift downwards in the low-redshift bin. In all cases, the best fits agree with our default results within 1σ. Fig. 11 shows the likelihood distributions for the fit with and without the hexadecapole. Including hexadecapoles reduces the uncertainties for all parameters in all redshift bins while maintaining the consistency in the constraints. This result agrees with our tests on mock catalogues as shown in Fig. 9.

The reduced χ^2 for the three fits is $79.3/(74 - 11) = 1.26$, $74.1/(74 - 11) = 1.18$ and $54.0/(74–11) = 0.86$ from low-to-high redshift, and the probability of having a reduced χ^2 value that exceeds this value is $Q = 8$ per cent, 16 per cent and 78 per cent, respectively. The increase in χ^2 for the lower redshift bins could arise because our model does not describe the low-redshift measurements as well as the high-redshift measurements due to the stronger non-linearity at low redshift. To test the sensitivity of the low redshift result on our modelling of non-linearity, we vary the choice of k_{max} and repeat the analysis using the fitting range $k = 0.01$–$0.13\,h\,\text{Mpc}^{-1}$ for the monopole and quadrupole, while we keep the fitting range of $k = 0.01$–$0.10\,h\,\text{Mpc}^{-1}$ for the hexadecapole. We obtain $f\sigma_8 = 0.470 \pm 0.066$, $F_{\text{AP}} = 0.422 \pm 0.023$ and $D_V r_{\text{s}}^{\text{fid}}/r_{\text{s}} = 1482 \pm 38$ Mpc, i.e. 15–30 per cent increase in the constraints by decreasing k_{max}. The reduced χ^2 of the best fit is $70.1/(66 - 11)$, i.e. the reduced χ^2 increases slightly from 1.26 to 1.27. Moreover, our best-fitting constraints are in good agreement with our results for the larger fitting range. We therefore conclude that the fitting constraints from the low-redshift bin are robust against the choice of k_{max}. Given that the probability of exceeding this χ^2 is still 8 per cent, the most likely explanation is a statistical fluctuation.

9 DISCUSSION

9.1 Power-spectrum multipoles

Fig. 10 compares the best-fitting power-spectra models with the data, where we indicate the NGC with filled data points and the SGC with open squares. The corresponding best-fitting models are indicated as a solid line for the NGC and a dashed line for the SGC. We use different nuisance parameters for the NGC and SGC, which makes the best-fitting models appear quite different, even though the underlying cosmology is the same. The need to have separate nuisance parameters for NGC and SGC is limited to the lowest redshift bin, where the two power spectra have different amplitudes in the monopole. The source of this difference is connected to chunks 2–6 (in NGC) that have a different target selection from the rest of the survey, leading to a lower density at low redshift (see Section 2, Reid et al. 2016 and Ross et al. 2016). The use of separate nuisance parameters for NGC and SGC does not degrade our parameter constraints and hence we used this approach for all redshift bins. The best-fitting models include the correction for the irregular μ-distribution as explained in Section 5.1.

The lower panels in Fig. 10 show the residual for the three multipoles. In the lowest redshift bin, the monopole data seem to prefer a systematically larger amplitude at small k, which the model does not appear to be able to accommodate given the constraints on large k. This might contribute to the overall larger χ^2 for this bin (see also the k_{max} test above). However, all fits result in reasonable reduced χ^2, indicating that the model is adequate in describing the data.

9.2 Parameter degeneracies and correlations

Here, we compare the correlation between different parameters with the theoretical expectation, with a focus on the second redshift bin. If we express the α value in $D_{\text{A}}(z)r_{\text{s}}^{\text{fid}}/r_{\text{s}}$ and $H(z)r_{\text{s}}/r_{\text{s}}^{\text{fid}}$, the following correlation matrix $(D_{\text{A}}(z)r_{\text{s}}^{\text{fid}}/r_{\text{s}}, H(z)r_{\text{s}}/r_{\text{s}}^{\text{fid}}, f\sigma_8)$ is produced:

$$\mathbf{R}_{z2}^{D_{\text{A}}-H} = \begin{pmatrix} 1 & 0.257 & 0.503 \\ 0.257 & 1 & 0.547 \\ 0.503 & 0.547 & 1 \end{pmatrix}. \tag{58}$$

---

[3] In reality, there is a small level of correlation between the different mocks; thus, our systematic bias is slightly overestimated.
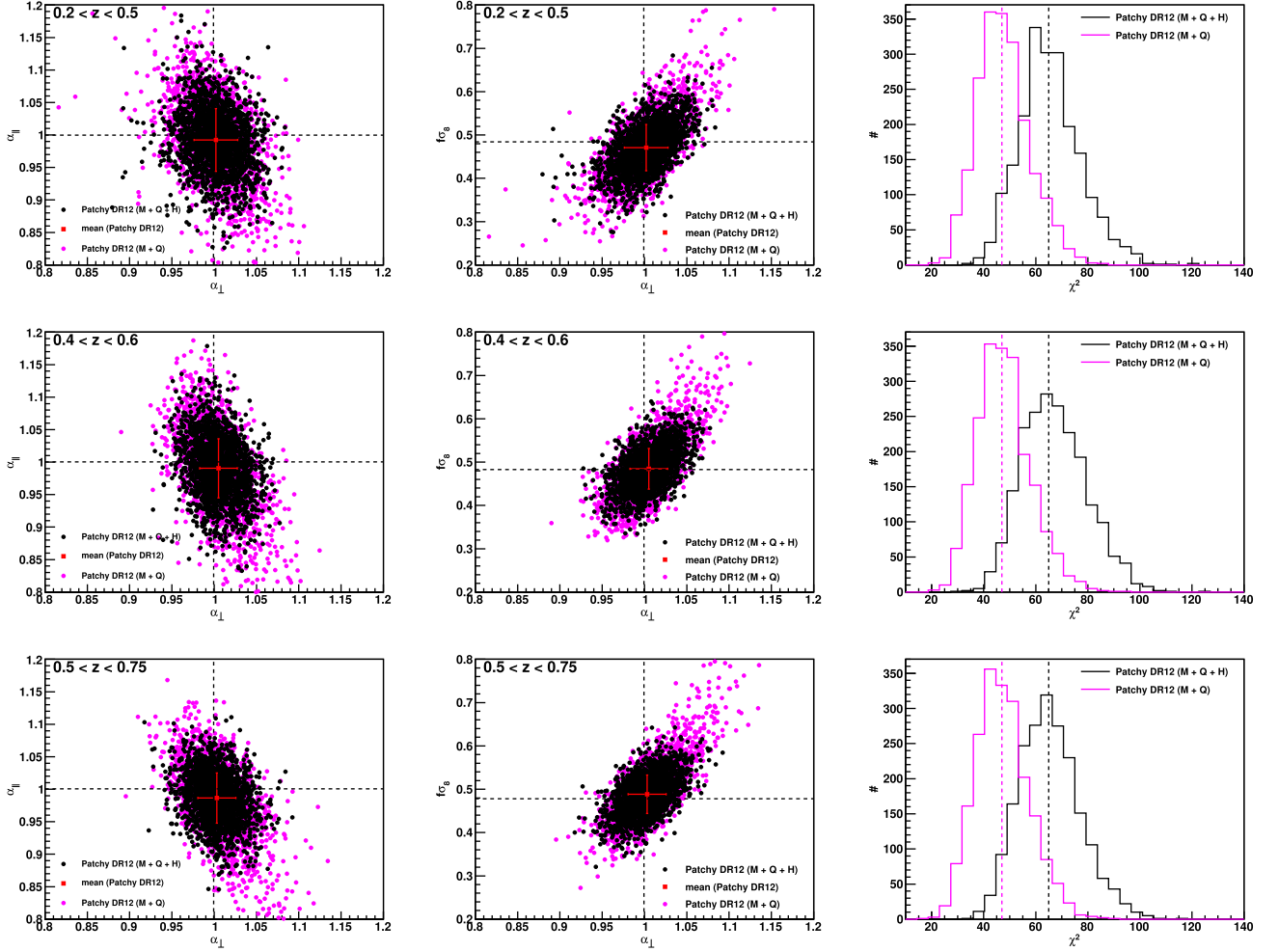
Figure 9. The maximum-likelihood results for all MultiDark-PATCHY mock catalogues. The black points show the results when fitting the monopole, quadrupole and hexadecapole with the fitting range $k = 0.01$–$0.15\,h\,\mathrm{Mpc}^{-1}$ for the monopole and quadrupole and $k = 0.01$–$0.10\,h\,\mathrm{Mpc}^{-1}$ for the hexadecapole. The magenta data points are the result of fits to only the monopole and quadrupole between $k = 0.01$ and $0.15\,h\,\mathrm{Mpc}^{-1}$. The red cross indicates the mean of the black points together with their variance. The histograms on the right show the corresponding χ^2 distributions, where the dashed lines indicate the degrees of freedom.

Table 2. The results for the fits to the MultiDark-PATCHY mock catalogues for the three redshift bins used in this analysis. For each bin, we show the result for the fit to the monopole, quadrupole and hexadecapole (M+Q+H) as well as the fit excluding the hexadecapole (M+Q). The fitting range is $k = 0.01$–$0.15\,h\,\mathrm{Mpc}^{-1}$ for the monopole and quadrupole and 0.01–$0.10\,h\,\mathrm{Mpc}^{-1}$ for the hexadecapole. The model to analyse the mock data is based on the BOSS fiducial cosmological model (see the end of Section 1) i.e. the α-values do not have to agree with unity. The expectation values for each redshift bin are given in the column labelled 'True'. The uncertainties represent the variance between all mock catalogues (not the error on the mean).

| | Test on mock catalogues | | | | | | | | |
| | $0.2 < z < 0.5$ | | | $0.4 < z < 0.6$ | | | $0.5 < z < 0.75$ | | |
	M+Q	M+Q+H	True	M+Q	M+Q+H	True	M+Q	M+Q+H	True
$f\sigma_8$	0.470 ± 0.073	0.471 ± 0.053	0.484	0.485 ± 0.068	0.484 ± 0.047	0.483	0.496 ± 0.068	0.488 ± 0.044	0.478
$\alpha_\parallel$	0.993 ± 0.065	0.992 ± 0.048	1.000	0.990 ± 0.065	0.990 ± 0.046	1.000	0.982 ± 0.060	0.987 ± 0.039	1.001
$\alpha_\perp$	1.001 ± 0.032	1.002 ± 0.025	0.999	1.005 ± 0.027	1.005 ± 0.022	0.999	1.006 ± 0.029	1.003 ± 0.022	0.999

The Fisher formalism (Seo & Eisenstein 2003, 2007; Shoji et al. 2009) predicts that if we understand RSD perfectly, the pure AP limit will give a correlation coefficient between $D_A(z)$ and $H(z)$ of 1 ($F_{AP} \propto D_A(z)H(z)$). If we increase the free parameters for RSD, the coefficient decreases. If we marginalize over all RSD informa-

tion and use the BAO alone, the expected correlation coefficient is -0.4. Therefore, for the BAO-only analysis, we expect $r \sim -0.4$ (see our companion paper Beutler et al. 2016b). Since we are using RSD as well as BAO information, we expect r somewhere between -0.4 and 1, depending on our freedom in RSD parameters. Our

Table 3. The best-fitting values for the three redshift bins in BOSS DR12. The results are also shown in Figs 10–12. The first section of the table shows the fit to the monopole, quadrupole and hexadecapole, while the second part excludes the hexadecapole. The fitting range is $k = 0.01$–$0.15\,h\,\mathrm{Mpc}^{-1}$ for the monopole and quadrupole and $k = 0.01$–$0.10\,h\,\mathrm{Mpc}^{-1}$ for the hexadecapole. We use separate nuisance parameters for the NGC and SGC. The parameters $F_{\mathrm{AP}} = (1 + z)D_{\mathrm{A}}H(z)/c$ and $D_V r_{\mathrm{s}}^{\mathrm{fid}}/r_{\mathrm{s}}$ are derived from $\alpha_\parallel$ and $\alpha_\perp$ following equations (48) and (49). The error bars are obtained by marginalizing over all other parameters.

		Monopole + quadrupole + hexadecapole					
		$0.2 < z < 0.5$ ($z_{\mathrm{eff}} = 0.38$)		$0.4 < z < 0.6$ ($z_{\mathrm{eff}} = 0.51$)		$0.5 < z < 0.75$ ($z_{\mathrm{eff}} = 0.61$)	
		Max. like.	Mean $\pm 1\sigma$	Max. like.	Mean $\pm 1\sigma$	Max. like.	Mean $\pm 1\sigma$
$\alpha_\parallel$		1.001	1.007 ± 0.037	1.007	1.015 ± 0.046	0.977	0.982 ± 0.040
$\alpha_\perp$		1.008	1.014 ± 0.027	1.014	1.015 ± 0.027	0.982	0.984 ± 0.024
$f(z)\sigma_8(z)$		0.478	0.482 ± 0.053	0.456	0.455 ± 0.050	0.412	0.410 ± 0.042
$\chi^2/\mathrm{d.o.f.}$		$79.3/(74-11)$	–	$74.1/(74-11)$	–	$54.0/(74-11)$	–
F_{AP}		0.426	0.427 ± 0.022	0.600	0.594 ± 0.035	0.732	0.736 ± 0.040
$D_V(z)r_{\mathrm{s}}^{\mathrm{fid}}/r_{\mathrm{s}}$	(Mpc)	1485	1493 ± 28	1908	1913 ± 35	2132	2133 ± 36
$H(z)r_{\mathrm{s}}/r_{\mathrm{s}}^{\mathrm{fid}}$	(km s^{-1} Mpc^{-1})	82.8	82.4 ± 3.0	89.0	88.5 ± 4.0	96.9	97.1 ± 3.9
$D_{\mathrm{A}}(z)r_{\mathrm{s}}^{\mathrm{fid}}/r_{\mathrm{s}}$	(Mpc)	1118	1124 ± 30	1331	1333 ± 35	1407	1410 ± 35
$b_1^{\mathrm{NGC}}\sigma_8$		1.339	1.336 ± 0.040	1.300	1.303 ± 0.040	1.230	1.235 ± 0.041
$b_1^{\mathrm{SGC}}\sigma_8$		1.337	1.332 ± 0.057	1.305	1.305 ± 0.046	1.259	1.247 ± 0.043
$b_2^{\mathrm{NGC}}\sigma_8$		1.16	$1.11^{+0.77}_{-0.89}$	2.08	$1.95^{+0.58}_{-0.66}$	2.83	$2.70^{+0.47}_{-0.54}$
$b_2^{\mathrm{SGC}}\sigma_8$		0.32	$0.52^{+0.64}_{-0.69}$	0.56	$0.61^{+0.60}_{-0.52}$	0.98	$0.71^{+0.55}_{-0.60}$
N^{NGC}		-1580	-1100^{+1410}_{-780}	-1710	-1555^{+620}_{-570}	-350	-350^{+950}_{-740}
N^{SGC}		-930	-500^{+1880}_{-1400}	-900	790^{+1000}_{-970}	-910	-130^{+860}_{-650}
σ_v^{NGC}		6.15	6.10 ± 0.69	5.84	$5.84^{+0.70}_{-0.77}$	5.39	$5.35^{+0.76}_{-0.81}$
σ_v^{SGC}		6.80	6.78 ± 0.83	6.39	6.46 ± 0.87	5.08	$4.93^{+0.88}_{-0.95}$
		Monopole + quadrupole					
		$0.2 < z < 0.5$ ($z_{\mathrm{eff}} = 0.38$)		$0.4 < z < 0.6$ ($z_{\mathrm{eff}} = 0.51$)		$0.5 < z < 0.75$ ($z_{\mathrm{eff}} = 0.61$)	
		Max. like.	Mean $\pm 1\sigma$	Max. like.	Mean $\pm 1\sigma$	Max. like.	Mean $\pm 1\sigma$
$\alpha_\parallel$		1.017	1.019 ± 0.045	0.982	0.982 ± 0.059	0.951	0.953 ± 0.046
$\alpha_\perp$		0.999	1.001 ± 0.030	1.025	1.031 ± 0.031	0.996	1.000 ± 0.027
$f(z)\sigma_8(z)$		0.457	0.459 ± 0.060	0.483	$0.494^{+0.071}_{-0.065}$	0.441	0.443 ± 0.054
$\chi^2/\mathrm{d.o.f.}$		$54.5/(56-11)$	–	$40.8/(56-11)$	–	$34.9/(56-11)$	–
F_{AP}		0.416	0.417 ± 0.027	0.619	0.626 ± 0.051	0.767	0.771 ± 0.052
$D_V(z)r_{\mathrm{s}}^{\mathrm{fid}}/r_{\mathrm{s}}$	(Mpc)	1484	1490 ± 28	1905	1912 ± 37	2129	2135 ± 37
$H(z)r_{\mathrm{s}}/r_{\mathrm{s}}^{\mathrm{fid}}$	(km s^{-1} Mpc^{-1})	81.5	81.5 ± 3.6	91.3	91.6 ± 5.6	100.1	100.1 ± 4.9
$D_{\mathrm{A}}(z)r_{\mathrm{s}}^{\mathrm{fid}}/r_{\mathrm{s}}$	(Mpc)	1107.7	1110 ± 33	1345.7	1354 ± 40	1427	1433 ± 39
$b_1^{\mathrm{NGC}}\sigma_8$		1.347	1.332 ± 0.047	1.289	1.283 ± 0.050	1.220	1.225 ± 0.045
$b_1^{\mathrm{SGC}}\sigma_8$		1.344	$1.335^{+0.55}_{-0.62}$	1.289	$1.271^{+0.049}_{-0.056}$	1.246	1.229 ± 0.046
$b_2^{\mathrm{NGC}}\sigma_8$		1.03	$0.84^{+0.78}_{-0.95}$	2.02	$1.48^{+0.64}_{-0.75}$	2.85	$2.66^{+0.45}_{-0.61}$
$b_2^{\mathrm{SGC}}\sigma_8$		0.32	0.6 ± 1.2	0.55	0.46 ± 0.63	0.93	$0.55^{+0.50}_{-0.61}$
N^{NGC}		1460	-600^{+1550}_{-750}	-1760	-1180 ± 1000	-380	-440^{+940}_{-760}
N^{SGC}		920	-600^{+3370}_{-1650}	-900	-70^{+1290}_{-860}	-910	20^{+860}_{-690}
σ_v^{NGC}		6.16	6.03 ± 0.73	5.75	5.67 ± 0.74	5.20	5.19 ± 0.74
σ_v^{SGC}		6.89	6.87 ± 0.81	6.20	6.06 ± 0.85	4.94	4.71 ± 0.85

value of $r = 0.257$ indicates a mixture of BAO and RSD information with a modest freedom in our RSD model. The most natural parametrization is given by $(D_V(z)r_{\mathrm{s}}^{\mathrm{fid}}/r_{\mathrm{s}}, F_{\mathrm{AP}}, f\sigma_8)$, which corresponds to the actual signals in the data. The correlation matrix is given by

$$\mathbf{R}_{z2}^{D_V-F_{\mathrm{AP}}} = \begin{pmatrix} 1 & -0.291 & -0.0562 \\ -0.291 & 1 & 0.648 \\ -0.0562 & 0.648 & 1 \end{pmatrix}. \tag{59}$$

There is a clear correlation between the AP parameter (F_{AP}) and growth rate $f\sigma_8$, while the BAO dilation parameter $D_V r_{\mathrm{s}}^{\mathrm{fid}}/r_{\mathrm{s}}$ and $f\sigma_8$ are almost uncorrelated. We include the correlation matrices, covariance matrices and inverse covariance matrices for these three parameters in Appendix B.

The correlation matrices indicate a correlation of about 60 per cent between F_{AP} and $f\sigma_8$. Therefore, if we hold F_{AP} fixed, i.e. if we assume that we know F_{AP} precisely, the constraints on $f\sigma_8$ can be significantly improved. This is an interesting case to consider, since when combining our results with the *Planck* constraints,
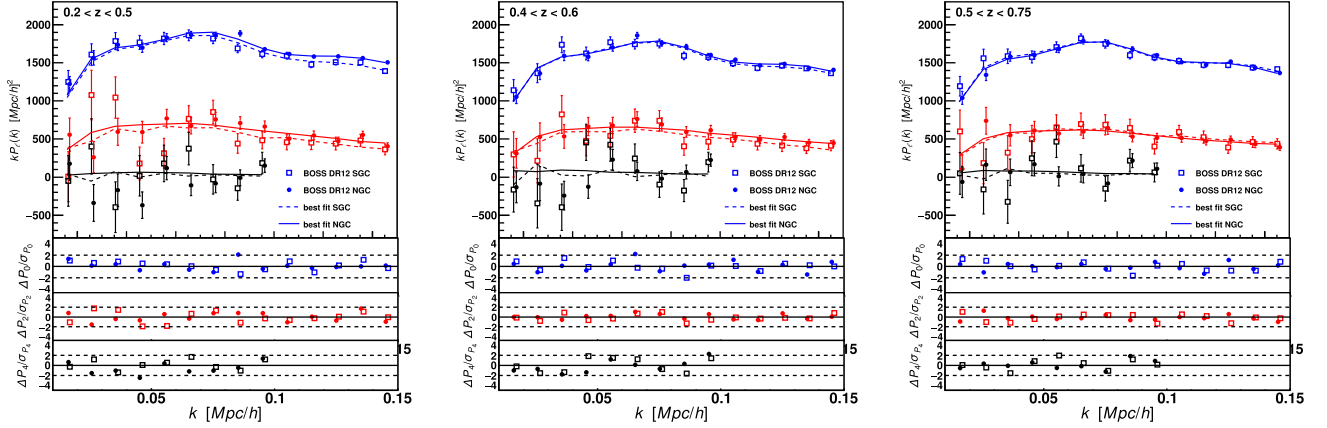
Figure 10. The best-fitting power-spectrum monopole (blue), quadrupole (red) and hexadecapole (black) models (lines) compared to the BOSS DR12 measurements (data points) in the three redshift bins used in this analysis. The measurements for the NGC are shown as filled circles, while the SGC data are displayed as open squares. The solid line represents the fit to the NGC, while the dashed line shows the result for the SGC. The best-fitting models include the irregular μ distribution effect as explained in equation (40), which is more prominent in the SGC since the volume is smaller. The NGC and SGC power spectra are fitted simultaneously for $f\sigma_8$, $\alpha_\parallel$ and $\alpha_\perp$, while we marginalize over different NGC and SGC nuisance parameters ($b_1\sigma_8$, $b_2\sigma_8$, N and σ_v). As a result, the best-fitting power spectra show different shapes for NGC and SGC, especially in the lowest redshift bin. The three lower panels show the residual for the three multipoles separately.
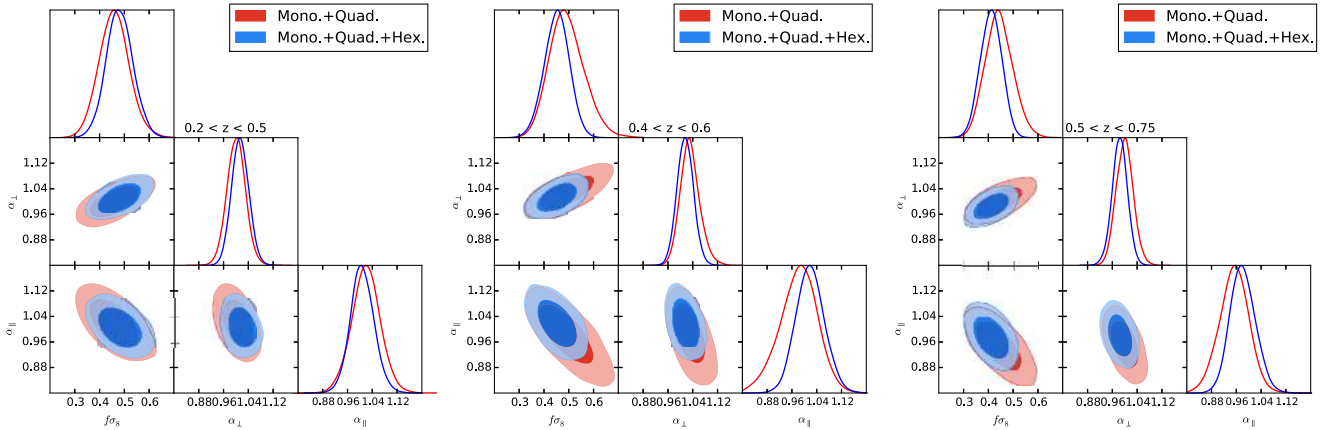
Figure 11. Likelihood distributions for the three redshift bins of BOSS DR12. We show the results for the parameters $\alpha_\perp$, $\alpha_\parallel$ and $f\sigma_8$. The blue contours use the monopole, quadrupole and hexadecapole, while the red contours exclude the hexadecapole. The fitting range is $k = 0.01$–$0.15\,h\,\mathrm{Mpc}^{-1}$ for the monopole and quadrupole, and $k = 0.01$–$0.10\,h\,\mathrm{Mpc}^{-1}$ for the hexadecapole. The numerical values are summarized in Table 3.

we effectively fix the background cosmological model. Fixing F_{AP} to the best-fitting value yields $f\sigma_8 = 0.482 \pm 0.037$, 0.455 ± 0.038 and 0.410 ± 0.034 for the low- ($z_{\mathrm{eff}} = 0.38$), middle- ($z_{\mathrm{eff}} = 0.51$) and high-redshift bin ($z_{\mathrm{eff}} = 0.61$), respectively.

9.3 Comparison to DR11 and other boss results

We compare these new results with our DR11 analysis (Beutler et al. 2014a). Our DR11 study found a growth of structure constraint of $f(z_{\mathrm{eff}})\sigma_8(z_{\mathrm{eff}}) = 0.419 \pm 0.043$ at $z_{\mathrm{eff}} = 0.57$, consistent with our high-redshift measurement in this analysis of $f(z_{\mathrm{eff}})\sigma_8(z_{\mathrm{eff}}) = 0.410 \pm 0.042$ at $z_{\mathrm{eff}} = 0.61$. Our new uncertainties are slightly larger compared to the DR11 result, which is caused by (1) the smaller redshift range given that our high-redshift bin has a low-redshift cut-off at 0.5 compared to 0.43 in the CMASS sample in Beutler et al. (2014a), and (2) the fact that we use different mock catalogues

compared to our DR11 analysis to generate the covariance matrix, which tend to result in larger uncertainties.

In Gil-Marín et al. (2016), the BOSS DR12 data have been analysed in Fourier space using the LOWZ and CMASS samples. They found a growth of structure constraint of $f(z_{\mathrm{eff}})\sigma_8(z_{\mathrm{eff}}) = 0.395 \pm 0.064$ at $z_{\mathrm{eff}} = 0.32$ and $f(z_{\mathrm{eff}})\sigma_8(z_{\mathrm{eff}}) = 0.442 \pm 0.037$ at $z_{\mathrm{eff}} = 0.57$ for LOWZ and CMASS, respectively. The LOWZ result is significantly (more than 1σ) smaller than our constraint in the low-redshift bin, which is $f(z_{\mathrm{eff}})\sigma_8(z_{\mathrm{eff}}) = 0.482 \pm 0.053$ at $z_{\mathrm{eff}} = 0.38$. There are many potential sources for this difference: (1) our low-redshift bin covers a redshift range of $z = 0.2$–0.5, which is slighter higher compared to the redshift range of $z = 0.2$–0.43 of LOWZ; (2) the additional data in our analysis (chunks 2–6) causes a difference in the target selection mainly in the low-redshift bin; (3) Gil-Marín et al. (2016) fit the power-spectrum monopole and quadrupole down to $k_{\mathrm{max}} = 0.24\,h\,\mathrm{Mpc}^{-1}$ compared to $k_{\mathrm{max}} = 0.15\,h\,\mathrm{Mpc}^{-1}$ in our analysis, which suggests that their constraint is dominated by high k
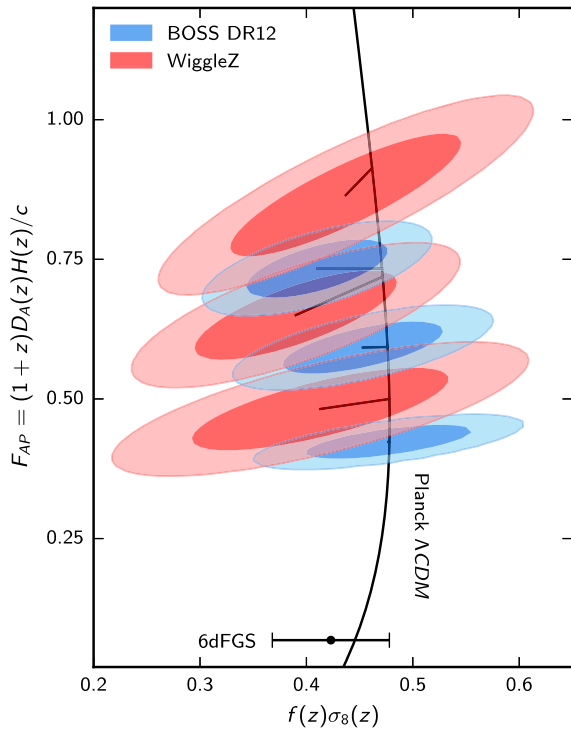
Figure 12. The constraints on the AP parameter (*y*-axis) and the growth of structure (*x*-axis). The *Planck* prediction for these values is shown as the black solid line, where we used the best-fitting ΛCDM model for the *Planck* data to extrapolate from the redshift of decoupling to low redshift. The red contours represent the results of the WiggleZ survey (Blake et al. 2012) at $z_{eff} = 0.44, 0.6$ and 0.73, and the black data point indicates the measurement in 6dFGS (Beutler et al. 2012) at $z_{eff} = 0.067$. Both parameters, $F_{AP}(z)$ and $f(z)\sigma_8(z)$, evolve with redshift and hence these contours at different z_{eff} are not expected to overlap. Short black lines connect the best-fitting values for each measurement with the *Planck* extrapolation for that particular redshift. The orientation of the degeneracy (i.e. the major axis of each contour ellipse) rotates with redshift, indicating that cosmological constraints can be improved by including measurements from many redshift bins.

modes; and (4) we include the hexadecapole in our analysis, which is not used in Gil-Marin et al. (2016).

The consistency between our results and our companion papers Sanchez et al. (2016), Grieb et al. (2016) and Satpathy et al. (2016) is discussed in Alam et al. (2016).

9.4 Comparison to other galaxy survey

Fig. 12 compares our measurements of the AP parameter and $f\sigma_8$ with measurements from the 6-degree Field Galaxy Survey (6dFGS; black data point; Beutler et al. 2012) at $z_{eff} = 0.067$ and the WiggleZ survey (red contours; Blake et al. 2012) at $z_{eff} = 0.44, 0.6$ and 0.73. The 6dFGS measurement ignored the AP effect by assuming that $D_A(z)$ and $H(z)$ are known, since the sensitivity to this signal becomes small at the 6dFGS redshift. The BOSS measurements cover a redshift range almost as wide as the WiggleZ measurement and with significantly reduced uncertainties. Given a smooth evolution of $f\sigma_8$ with redshift, the WiggleZ and BOSS measurements are consistent with each other.[4]

---

[4] Note that there is a small level of correlation between these two surveys (Beutler et al. 2016a; Marin et al. 2016).

The only large-scale structure analysis in the literature we are aware of, which makes use of the hexadecapole, is the study by Oka et al. (2014), which, however, ignores all window-function effects. Our analysis suggests that the window-function effects in the hexadecapole are indeed negligible when compared to the measurement uncertainties, while the effects of the window function on the monopole and quadrupole are significant; ignoring these effects would significantly bias our results.

9.5 Comparison to *Planck* 2015

Next, we can compare our measurements to the *Planck* 2015 results (Planck Collaboration XIII 2016). Using a ΛCDM model to extrapolate from the redshift of decoupling to the effective redshifts of our large-scale-structure measurements, *Planck* predicts values for the growth of structure of $f(z_{eff})\sigma_8(z_{eff}) = 0.4784 \pm 0.0077$, 0.4763 ± 0.0060 and 0.4707 ± 0.0058 for the low- ($z_{eff} = 0.38$), middle- ($z_{eff} = 0.51$) and high-redshift bins ($z_{eff} = 0.61$), respectively. The largest deviation between our measurements and the *Planck* ΛCDM predictions occurs at the highest redshift bin, where our value is lower than *Planck* by about 1.4σ. Fig. 12 compares our two-dimensional constraints on the growth of structure and the AP effect with the *Planck* ΛCDM predictions for these parameters. The deviation of the highest redshift data point is not statistically significant. Together with our low-redshift measurements, which agree well with the *Planck* predictions, there is overall good consistency between the RSD constraints from BOSS and the *Planck* data set.

10 CONCLUSIONS

We measure the power-spectrum multipoles from the final BOSS DR12 data set in the redshift range $0.2 < z < 0.75$. We extract the BAO, AP and RSD signals using a model based on renormalized perturbation theory. For the first time, we include the hexadecapole in our analysis, while appropriately accounting for the survey window function, which reduced the uncertainties on $f(z)\sigma_8(z)$ by about 20 per cent. The main results of this analysis are as follows.

(i) An FFT-based window-function method, first suggested in Wilson et al. (2015) using the global plane-parallel approximation, can be derived within the local plane-parallel approximation, which makes it applicable to wide-angle surveys like BOSS. We present the detailed derivation in Appendix A.

(ii) By fitting the monopole and quadrupole between $k = 0.01$ and $0.15\,h\,\mathrm{Mpc}^{-1}$ and the hexadecapole between $k = 0.01$ and $0.10\,h\,\mathrm{Mpc}^{-1}$, we were able to extract the constraints $f(z_{eff})\sigma_8(z_{eff}) = 0.482 \pm 0.053, 0.455 \pm 0.050$ and 0.410 ± 0.042 at the effective redshifts of $z_{eff} = 0.38, 0.51$ and 0.61, respectively. For the AP parameter $F_{AP} = (1 + z_{eff})D_A(z_{eff})H(z_{eff})/c$, we find 0.427 ± 0.022, 0.594 ± 0.035 and 0.736 ± 0.040 and the BAO scale parameter is $D_V r_s^{fid}/r_s = 1493 \pm 28, 1913 \pm 35$ and $2133 \pm 36\,\mathrm{Mpc}$. Assuming Gaussian likelihood, we provide a covariance matrix that contains the parameter constraints as well as their correlations (see Appendix B).

(iii) We demonstrated the accuracy of our analysis pipeline by participating in a mock challenge, which resulted in systematic uncertainties $\lesssim 10$ per cent of the statistical error budget. The description of this mock challenge can be found in our companion paper (Tinker et al. 2016).

(iv) Our high-redshift result on $f\sigma_8$ is in agreement with our DR11 analysis using the CMASS sample, and shows a small 1.4σ deviation from the *Planck* prediction. The low-redshift results

obtained in this analysis show good agreement with the *Planck* prediction.

Alam et al. (2016) combine our measurements with the corresponding growth of structure measurements of Grieb et al. (2016), Sanchez et al. (2016) and Satpathy et al. (2016) and the BAO-only measurements of Beutler et al. (2016b) and Ross et al. (2016) into a final BOSS likelihood and investigate the cosmological implications.

REFERENCES

Alam S. et al., 2015, ApJS, 219, 12
Alam et al., 2016
Alcock C., Paczynski B., 1979, Nature, 281, 358
Anderson L. et al., 2014, MNRAS, 441, 24
Baldauf T., Seljak U., Desjacques V., McDonald P., 2012, Phys. Rev. D, 86, 083540
Ballinger W. E., Peacock J. A., Heavens A. F., 1996, MNRAS, 282, 877
Beutler F. et al., 2011, MNRAS, 416, 3017
Beutler F. et al., 2012, MNRAS, 423, 3430
Beutler F. et al., 2014a, MNRAS, 443, 1065
Beutler F. et al., 2014b, MNRAS, 444, 3501
Beutler F., Blake C., Koda J., Marin F., Seo H. J., Cuesta A. J., Schneider D. P., 2016a, MNRAS, 455, 3230
Beutler F. et al., 2016b
Biagetti M., Chan K. C., Desjacques V., Paranjape A., 2014, MNRAS, 441, 1457
Bianchi D., Gil-Mar n H., Ruggeri R., Percival W. J., 2015, MNRAS, 453, L11
Blake C. et al., 2011, MNRAS, 415, 2876
Blake C. et al., 2012, MNRAS, 425, 405
Bolton A. S. et al., 2012, AJ, 144, 144
Bundy K. et al., 2015, ApJ, 798, 7
Chuang C.-H. et al., 2013, MNRAS, 433, 3559
Dawson K. S. et al., 2013, AJ, 145, 10
Doi M. et al., 2010, AJ, 139, 1628
Eisenstein D. J., Seo H. J., Sirko E., Spergel D., 2007, ApJ, 664, 675
Eisenstein D. J. et al., 2011, AJ, 142, 72
Feldman H. A., Kaiser N., Peacock J. A., 1994, ApJ, 426, 23
Foreman-Mackey D., Hogg D. W., Lang D., Goodman J., 2013, PASJ, 125, 306
Fukugita M., Ichikawa T., Gunn J. E., Doi M., Shimasaku K., Schneider D. P., 1996, AJ, 111, 1748
Garilli B. et al., 2014, A&A, 562, A23
Gelman A., Rubin D. B., 1992, Stat. Sci., 7, 457
Gil-Marin H. et al., 2016, MNRAS, 460, 4188
Grieb J. N. et al., 2016
Gunn J. E. et al., 1998, AJ, 116, 3040
Gunn J. E. et al., 2006, AJ, 131, 2332
Guo H., Zehavi I., Zheng Z., 2012, ApJ, 756, 127
Guzzo L. et al., 2008, Nature, 451, 541
Hartlap J., Simon P., Schneider P., 2007, A&A, 464, 399
Hawkins E. et al., 2003, MNRAS, 346, 78
Jing Y. P., 2005, ApJ, 620, 559
Kaiser N., 1987, MNRAS, 227, 1
Kitaura F. S. et al., 2016, MNRAS, 456, 4156
Klypin A., Yepes G., Gottlober S., Prada F., Heß S., 2016, MNRAS, 457, 4340
Lazeyras T., Wagner C., Baldauf T., Schmidt F., 2016, J. Cosmol. Astropart. Phys., 1602, 018
Leauthaud A. et al., 2016, MNRAS, 457, 4021
Lesgourgues J., Pastor S., 2006, Phys. Rep., 429, 307
Lewandowski M., Senatore L., Prada F., Zhao C., Chuang C. H., 2015, preprint (arXiv:1512.06831)
Li Y., Hu W., Takada M., 2016, Phys. Rev. D, 93, 063507
McDonald P., Roy A., 2009, J. Cosmol. Astropart. Phys., 0908, 020
Marin F. A., Beutler F., Blake C., Koda J., Kazin E., Schneider D. P., 2016, MNRAS, 455, 4046
Matsubara T., Suto Y., 1996, ApJ, 470, L1
Nishimichi T., Oka A., 2014, MNRAS, 444, 1400
Oka A., Saito S., Nishimichi T., Taruya A., Yamamoto K., 2014, MNRAS, 439, 2515
Okumura T., Matsubara T., Eisenstein D. J., Kayo I., Hikage C., Szalay A. S., Schneider D. P., 2008, ApJ, 676, 889
Okumura T., Hand N., Seljak U., Vlah Z., Desjacques V., 2015, Phys. Rev. D, 92, 103516
Padmanabhan N., White M. J., 2008, Phys. Rev. D, 77, 123540
Peacock J. A. et al., 2001, Nature, 410, 169
Percival W. J. et al., 2014, MNRAS, 439, 2531
Planck Collaboration XIII, 2016, A&A, 594, A13
Reid B. A. et al., 2012, MNRAS, 426, 2719
Reid B. et al., 2016, MNRAS, 455, 1553
Rodrguez-Torres S. A. et al., 2016, MNRAS, 460, 1173
Ross A. J. et al., 2012, MNRAS, 424, 564
Ross A. J. et al., 2016
Saito S., Baldauf T., Vlah Z., Seljak U., Okumura T., McDonald P., 2014, Phys. Rev. D, 90, 123522

Saito S. et al., 2016, MNRAS, 460, 1457

Samushia L., Percival W. J., Raccanelli A., 2012, MNRAS, 420, 2102

Samushia L. et al., 2013, MNRAS, 429, 1514

Sanchez A. G. et al., 2016

Satpathy et al., 2016

Schmidt F., 2016, Phys. Rev. D, 93, 063512

Scoccimarro R., 2004, Phys. Rev. D, 70, 083007

Scoccimarro R., 2015, Phys. Rev. D, 92, 083532

Sefusatti E., Crocce M., Scoccimarro R., Couchman H., 2016, MNRAS, 460, 3624

Seo H.-J., Eisenstein D. J., 2003, ApJ, 598, 720

Seo H. J., Eisenstein D. J., 2007, ApJ, 665, 14

Shoji M., Jeong D., Komatsu E., 2009, ApJ, 693, 1404

Smee S. et al., 2013, AJ, 126, 32

Smith J. A. et al., 2002, AJ, 123, 2121

Taruya A., Nishimichi T., Saito S., 2010, Phys. Rev. D, 82, 063522 (TNS)

Taruya A., Bernardeau F., Nishimichi T., Codis S., 2012, Phys. Rev. D, 86, 103528

Tegmark M. et al., 2006, Phys. Rev. D, 74, 123507

Tinker J. L. et al., 2016

Vargas-Magana et al., 2016

Wilson M. J., Peacock J. A., Taylor A. N., de la Torre S., 2015, preprint (arXiv:1511.07799)

Yamamoto K., Nakamichi M., Kamino A., Bassett B. A., Nishioka H., 2006, PASJ, 58, 93

Yamamoto K., Sato T., Huetsi G., 2008, Prog. Theor. Phys. 120, 609

Yoo J., Seljak U., 2015, MNRAS, 447, 1789

Zheng Y., Song Y. S., 2016, J. Cosmol. Astropart. Phys., 08, 050

APPENDIX A: WINDOW FUNCTION

Here, we describe the inclusion of the survey window-function effects in our power-spectrum model. First we will discuss the convolution of the power-spectrum model with the window function, followed by the integral-constraint effect. We also show a rederivation of the window-function formalism of Wilson et al. (2015) using the local plain-parallel approximation (instead of the global plain-parallel approximation as in Wilson et al. 2015); this approach allows the application of this method to wide-angle surveys like BOSS.

A1 Derivation within the local plane-parallel approximation

The convolved correlation function multipoles can be expressed as

$$\hat{\xi}_\ell(s) = \frac{2\ell+1}{2} \int d\mu_s \int \frac{d\phi}{2\pi} \xi(s) W^2(s) \mathcal{L}_\ell(\hat{s} \cdot \hat{x}_h), \tag{A1}$$

where $\mathcal{L}_\ell$ is the Legendre polynomial of order ℓ and $\xi(s)$ and $W^2(s)$ are the anisotropic correlation function and window function, respectively:

$$\xi(s) = \sum_L \xi_L(s) \mathcal{L}_L(\mu_s) \tag{A2}$$

and

$$W^2(s) = \int dx_1 W(x_1) W(x_1 + s) = \sum_p W_p^2(s) \mathcal{L}_p(\mu_s). \tag{A3}$$

Here, $s = x_2 - x_1$ is the pair separation vector, and μ_s is the cosine of the angle of the separation vector relative to the line of sight, i.e. $\mu_s = \hat{s} \cdot \hat{x}_h$, where $x_h = (x_1 + x_2)/2 = x_1 + s/2$ is known as the local plane-parallel approximation (see Beutler et al. 2014a, section 3.1). The window-function multipoles $W_p^2(s)$ are given by

$$W_p^2(s) = \frac{2p+1}{2} \int d\mu_s \int \frac{d\phi}{2\pi} \int dx_1 W(x_1) W(x_1 + s) \mathcal{L}_\ell(\mu_s). \tag{A4}$$

Multipole expanding the correlation function and window function in equation (A1) produces

$$\hat{\xi}_\ell(s) = \frac{2\ell+1}{2} \int d\mu_s \sum_L \xi_L(s) \mathcal{L}_L(\mu_s)$$
$$\sum_p W_p^2(s) \mathcal{L}_p(\mu_s) \mathcal{L}_\ell(\mu_s). \tag{A5}$$

Using the relation

$$\mathcal{L}_\ell \mathcal{L}_p = \sum_t a_{pt}^\ell \mathcal{L}_t, \tag{A6}$$

leads to

$$\hat{\xi}_\ell(s) = \frac{2\ell+1}{2} \int d\mu_s \int \frac{d\phi}{2\pi} \sum_L \xi_L(s) \sum_p W_p^2(s)$$
$$\times \sum_t a_{Lt}^\ell \mathcal{L}_t(\mu_s) \mathcal{L}_p(\mu_s). \tag{A7}$$

We can further simplify this expression using the integral relation

$$\int d\mu_s \int \frac{d\phi}{2\pi} \mathcal{L}_p(\mu_s) \mathcal{L}_t(\mu_s) = \frac{2}{2p+1} \delta_{pt} \tag{A8}$$

to find

$$\hat{\xi}_\ell(s) = (2\ell+1) \sum_L \xi_L(s) \sum_p \frac{1}{2p+1} W_p^2(s) a_{Lp}^\ell. \tag{A9}$$

To determine the coefficients a_{Lp}^ℓ, we use equation (A6), multiply the polynomial expressions for the Legendre polynomials on the left, and use

$$\mu^n = \sum_{\ell=n,(n-1),\dots} \frac{(2\ell+1)n! \mathcal{L}_\ell(\mu_s)}{2^{(n-\ell)/2}(\frac{1}{2}(n-\ell))!(\ell+n+1)!!}. \tag{A10}$$

Equation (A9) is fairly straightforward to evaluate for any model correlation function $\xi_\ell(s)$. The window-function multipoles can be calculated from the random pair counts $RR(s, \mu_s)$ as

$$W_\ell^2(s) \propto \sum_{\mu_s} \sum_{x_1} \sum_{x_2} RR(s, \mu_s) \mathcal{L}_\ell(\mu_s), \tag{A11}$$

where the normalization is chosen as $W_\ell^2(s \to 0) = 1$ for $\ell = 0$.

Now we want to include the simple window-function treatment in configuration space into our Fourier-space model. The observed power spectrum is

$$\hat{P}(k) = \int dx_1 \int dx_2 \langle \delta(x_1)\delta(x_2)W(x_1)W(x_2) \rangle e^{ik \cdot x_1} e^{-ik \cdot x_2}$$
$$= \int dx_1 \int ds \langle \delta(x_1)\delta(x_1 + s) \rangle$$
$$\times W(x_1)W(x_1 + s)e^{ik \cdot x_1} e^{-ik \cdot (x_1+s)} \tag{A12}$$

$$= \int dx_1 \int ds \, \xi(s) W(x_1) W(x_1 + s) e^{-ik \cdot s} \tag{A13}$$

$$= \int dx_1 \int ds \left(\sum_L \xi_L(s) \mathcal{L}_L(\hat{x}_h \cdot \hat{s}) \right)$$
$$\times W(x_1) W(x_1 + s) e^{-ik \cdot s}, \tag{A14}$$

where we used

$$\langle \delta(x_1)\delta(x_1 + s)W(x_1)W(x_1 + s) \rangle$$
$$= \langle \delta(x_1)\delta(x_1 + s) \rangle W(x_1)W(x_1 + s). \tag{A15}$$

The multipole moment power spectrum in the local plain-parallel approximation is then

$$
\hat{P}_\ell(k) = \frac{2\ell+1}{2} \int d\mu_k \int \frac{d\phi}{2\pi} \int d\boldsymbol{x}_1 \int d\boldsymbol{x}_2 e^{i\boldsymbol{k}\cdot\boldsymbol{x}_1} e^{-i\boldsymbol{k}\cdot\boldsymbol{x}_2}
$$
$$
\times \langle \delta(\boldsymbol{x}_1)\delta(\boldsymbol{x}_2)W(\boldsymbol{x}_1)W(\boldsymbol{x}_2)\rangle \mathcal{L}_\ell(\hat{\boldsymbol{k}}\cdot\hat{\boldsymbol{x}}_h)
$$

$$
= \frac{2\ell+1}{2} \int d\mu_k \int \frac{d\phi}{2\pi} \int d\boldsymbol{x}_1 \int d\boldsymbol{s}
$$
$$
\times \left(\sum_L \xi_L(s)\mathcal{L}_L(\hat{\boldsymbol{x}}_h \cdot \hat{\boldsymbol{s}}) \right)
$$
$$
\times W(\boldsymbol{x}_1)W(\boldsymbol{x}_1+\boldsymbol{s})e^{-i\boldsymbol{k}\cdot\boldsymbol{s}}\mathcal{L}_\ell(\hat{\boldsymbol{k}}\cdot\hat{\boldsymbol{x}}_h), \tag{A16}
$$

where $\int d\mu_k$ represents the integration over all the possible cosine angles between $\hat{\boldsymbol{k}}$ and $\hat{\boldsymbol{x}}_h$. Now, we apply the relations

$$
e^{i\boldsymbol{k}\cdot\boldsymbol{s}} = \sum_p (-i)^p (2p+1) j_p(ks)\mathcal{L}_p(\hat{\boldsymbol{k}}\cdot\hat{\boldsymbol{s}}), \tag{A17}
$$

and

$$
\int d\mu_k \int \frac{d\phi}{2\pi}\mathcal{L}_\ell(\hat{\boldsymbol{k}}\cdot\hat{\boldsymbol{x}}_h)\mathcal{L}_p(\hat{\boldsymbol{k}}\cdot\hat{\boldsymbol{s}}) = \frac{2}{2\ell+1}\mathcal{L}_\ell(\hat{\boldsymbol{s}}\cdot\hat{\boldsymbol{x}}_h)\delta_{\ell p}, \tag{A18}
$$

which allows us to express the multipole power spectra as

$$
\hat{P}_\ell(k) = \frac{2\ell+1}{2} \int d\mu_k \int \frac{d\phi}{2\pi} \int d\boldsymbol{x}_1 \int d\boldsymbol{s}
$$
$$
\times \sum_L \xi_L(s) \sum_p i^p(2p+1)j_p(ks)
$$
$$
\times W(\boldsymbol{x}_1)W(\boldsymbol{x}_1+\boldsymbol{s})\mathcal{L}_\ell(\hat{\boldsymbol{k}}\cdot\hat{\boldsymbol{x}}_h)\mathcal{L}_p(\hat{\boldsymbol{k}}\cdot\hat{\boldsymbol{s}})\mathcal{L}_L(\hat{\boldsymbol{x}}_h\cdot\hat{\boldsymbol{s}}) \tag{A19}
$$

$$
= \int d\boldsymbol{x}_1 \int d\boldsymbol{s} \sum_L \xi_L(s)i^\ell(2\ell+1)j_\ell(ks)
$$
$$
\times W(\boldsymbol{x}_1)W(\boldsymbol{x}_1+\boldsymbol{s})\mathcal{L}_\ell(\hat{\boldsymbol{x}}_h\cdot\hat{\boldsymbol{s}})\mathcal{L}_L(\hat{\boldsymbol{x}}_h\cdot\hat{\boldsymbol{s}}). \tag{A20}
$$

Using $\mathcal{L}_\ell\mathcal{L}_L = \sum_t a_{Lt}^\ell\mathcal{L}_t$ (from equation A6) leads to

$$
\hat{P}_\ell(k) = \int d\boldsymbol{s} \sum_L \xi_L(s)i^\ell(2\ell+1)j_\ell(ks)
$$
$$
\times \int d\boldsymbol{x}_1 W(\boldsymbol{x}_1)W(\boldsymbol{x}_1+\boldsymbol{s})\sum_t a_{Lt}^\ell\mathcal{L}_t(\hat{\boldsymbol{x}}_h\cdot\hat{\boldsymbol{s}}) \tag{A21}
$$

$$
= \int 2\pi s^2 ds \sum_L \xi_L(s)i^\ell(2\ell+1)j_\ell(ks)
$$
$$
\times \sum_t a_{Lt}^\ell \int d\mu_s \int \frac{d\phi}{2\pi} \int d\boldsymbol{x}_1
$$
$$
\times W(\boldsymbol{x}_1)W(\boldsymbol{x}_1+\boldsymbol{s})\mathcal{L}_t(\hat{\boldsymbol{x}}_h\cdot\hat{\boldsymbol{s}}). \tag{A22}
$$

Using the definition of the window-function multipoles of equation (A4), we can write the equation above as

$$
\hat{P}_\ell(k) = i^\ell(2\ell+1)\int 2\pi s^2 ds\, j_\ell(ks)
$$
$$
\times \sum_L \sum_t \frac{2}{2t+1}a_{Lt}^\ell\xi_L(s)W_t^2(s). \tag{A23}
$$

Substituting with equation (A9), the convolved power-spectrum multipoles are given by

$$
\hat{P}_\ell(k) = 4\pi i^\ell \int ds\, s^2\hat{\xi}_\ell(s)j_\ell(sk). \tag{A24}
$$

For our analysis, we need to calculate the convolved monopole, quadrupole and hexadecapole power spectra. Therefore, the convolved correlation function multipoles in equation (18), relevant for our analysis, are given by

$$
\hat{\xi}_0(s) = \xi_0 W_0^2 + \frac{1}{5}\xi_2 W_2^2 + \frac{1}{9}\xi_4 W_4^2 + \cdots \tag{A25}
$$

$$
\hat{\xi}_2(s) = \xi_0 W_2^2 + \xi_2\left[W_0^2 + \frac{2}{7}W_2^2 + \frac{2}{7}W_4^2\right]
$$
$$
+ \xi_4\left[\frac{2}{7}W_2^2 + \frac{100}{693}W_4^2 + \frac{25}{143}W_6^2\right]
$$
$$
+ \cdots \tag{A26}
$$

$$
\hat{\xi}_4(s) = \xi_0 W_4^2 + \xi_2\left[\frac{18}{35}W_2^2 + \frac{20}{77}W_4^2 + \frac{45}{143}W_6^2\right]
$$
$$
+ \xi_4\left[W_0^2 + \frac{20}{77}W_2^2 + \frac{162}{1001}W_4^2\right.
$$
$$
\left. + \frac{20}{143}W_6^2 + \frac{490}{2431}W_8^2\right]
$$
$$
+ \cdots \tag{A27}
$$

We truncate the formula after the hexadecapole contribution of the correlation function, but use all window-function multipoles up to $\ell = 8$.

A2 The integral-constraint correction

Whenever we estimate a power spectrum, we must make an assumption of the mean density of the Universe, so that we can properly define an overdensity field. The standard assumption is that the mean density of the Universe is equivalent to the mean density of the survey. The non-zero sample variance expected at the wavelengths that correspond to the size of the survey invalidates this assumption. In general, this assumption affects only the mean density, i.e. forcing the power spectrum near $k = 0$ to be zero, which is known as the integral constraint. However, the window function correlates various modes with $k = 0$ and therefore propagates the incorrect estimation of $k = 0$ to other scales that are relevant for cosmological measurements. Equations (19) and (20) demonstrate how the integral constraint affects the correlation function. Without the window-function effect, i.e. $W_0 = 1$ with $W_{\ell \geq 2} = 0$, the integral constraint will simply introduce a constant offset to $\xi_0(s)$ and therefore to $\hat{\xi}_0(s)$. With scale-dependent non-zero W_0 and W_2 however, a constant offset in $\xi_0(s)$ becomes scale-dependent in $\hat{\xi}_0(s)$ and $\hat{\xi}_2(s)$, affecting the shape of the correlation function.

We can account for the integral-constraint bias by correcting the model power spectrum as

$$
P_\ell^{\text{ic-corrected}}(k) = \hat{P}_\ell(k) - P_0 W_\ell^2(k), \tag{A28}
$$

where the window functions $W_\ell^2(k)$ can be obtained from $W^2(s)$ defined in equation (22) as

$$
W_\ell^2(k) = 4\pi \int ds\, s^2 W_\ell^2(s)j_\ell(sk). \tag{A29}
$$

The integral-constraint correction in BOSS only affects modes $\lesssim 0.005\, h\,\text{Mpc}^{-1}$ and does not affect any of our results.

APPENDIX B: CORRELATION, COVARIANCE AND INVERSE COVARIANCE MATRICES

We determine the correlation between the three cosmological parameter constraints $(D_V(z)r_s^{\mathrm{fid}}/r_s,\ F_{\mathrm{AP}},\ f\sigma_8)$ using the MultiDark-PATCHY mock catalogues. This approach leads to the following correlation matrix for the first redshift bin

$$
\mathbf{R}_{z1} = \begin{pmatrix} 1 & -0.206 & 0.0490 \\ -0.206 & 1 & 0.652 \\ 0.0490 & 0.652 & 1 \end{pmatrix}, \tag{B1}
$$

which leads to a covariance matrix of

$$
\mathbf{C}_{z1} = \begin{pmatrix} 1090 & -0.136 & 0.0825 \\ -0.136 & 0.000\,400 & 0.000\,665 \\ 0.0825 & 0.000\,665 & 0.002\,60 \end{pmatrix} \tag{B2}
$$

and the inverse of this matrix is

$$
\mathbf{C}_{z1}^{-1} = \begin{pmatrix} 0.001\,02 & 0.697 & -0.211 \\ 0.697 & 4830 & -1260 \\ -0.211 & -1260 & 713 \end{pmatrix}. \tag{B3}
$$

For the second redshift bin, we find

$$
\mathbf{R}_{z2} = \begin{pmatrix} 1 & -0.291 & -0.056 \\ -0.291 & 1 & 0.648 \\ -0.056 & 0.648 & 1 \end{pmatrix} \tag{B4}
$$

and the covariance matrix is

$$
\mathbf{C}_{z2} = \begin{pmatrix} 1940 & -0.397 & -0.124 \\ -0.397 & 0.000\,961 & 0.001\,00 \\ -0.124 & 0.001\,00 & 0.002\,50 \end{pmatrix}. \tag{B5}
$$

Inverting this matrix yields

$$
\mathbf{C}_{z2}^{-1} = \begin{pmatrix} 0.000\,582 & 0.360 & -0.115 \\ 0.360 & 2010 & -784 \\ -0.115 & -784 & 708 \end{pmatrix}. \tag{B6}
$$

Finally, for the third redshift bin, we have

$$
\mathbf{R}_{z3} = \begin{pmatrix} 1 & -0.126 & 0.101 \\ -0.126 & 1 & 0.619 \\ 0.101 & 0.619 & 1 \end{pmatrix} \tag{B7}
$$

and

$$
\mathbf{C}_{z3} = \begin{pmatrix} 2120 & -0.197 & 0.205 \\ -0.197 & 0.001\,16 & 0.000\,927 \\ 0.205 & 0.000\,927 & 0.001\,94 \end{pmatrix}. \tag{B8}
$$

The inverse matrix is

$$
\mathbf{C}_{z3}^{-1} = \begin{pmatrix} 0.000\,506 & 0.208 & -0.153 \\ 0.208 & 1480 & -729 \\ -0.153 & -729 & 880 \end{pmatrix}. \tag{B9}
$$

Only the first and second redshift bins are independent, while the middle redshift bin is correlated with the other two. These results can be used together with the data vector for any likelihood analysis, e.g. for the first redshift bin the data vector is $\boldsymbol{D}_{z1} = (1485, 0.426, 0.478)$ and the corresponding likelihood is $\mathcal{L}_{z1} = D_{z1}^{\mathrm{T}} \mathbf{C}_{z1}^{-1} D_{z1}$.

[1]*Institute of Cosmology & Gravitation, Dennis Sciama Building, University of Portsmouth, Portsmouth PO1 3FX, UK*
[2]*Lawrence Berkeley National Lab, 1 Cyclotron Rd, Berkeley, CA 94720, USA*
[3]*Department of Physics and Astronomy, Ohio University, 251B Clippinger Labs, Athens, OH 45701, USA*
[4]*Kavli Institute for the Physics and Mathematics of the Universe (WPI), The University of Tokyo Institutes for Advanced Study, The University of Tokyo, Kashiwa, Chiba 277-8583, Japan*
[5]*Max-Planck-Institut für Astrophysik, Karl-Schwarzschild-Strasse 1, D-85740 Garching bei München, Germany*
[6]*Instituto de Física Teórica, (UAM/CSIC), Universidad Autónoma de Madrid, Cantoblanco, E-28049 Madrid, Spain*
[7]*Leibniz-Institut für Astrophysik Potsdam (AIP), An der Sternwarte 16, D-14482 Potsdam, Germany*
[8]*Institut de Ciències del Cosmos (ICCUB), Universitat de Barcelona (IEEC-UB), Martí i Franquès 1, E-08028 Barcelona, Spain*
[9]*Harvard–Smithsonian Center for Astrophysics, 60 Garden St, Cambridge, MA 02138, USA*
[10]*Sorbonne Universités, Institut Lagrange de Paris (ILP), 98 bis Boulevard Arago, F-75014 Paris, France*
[11]*Laboratoire de Physique Nuclaire et de Hautes Energies, Université Pierre et Marie Curie, 4 Place Jussieu, F-75005 Paris, France*
[12]*Max-Planck-Institut für extraterrestrische Physik, Postfach 1312, Giessenbachstr., D-85741 Garching, Germany*
[13]*Universitäts-Sternwarte München, Ludwig-Maximilians-Universität München, Scheinerstraße 1, D-81679 München, Germany*
[14]*Department of Astronomy, University of California, Berkeley, CA 94720, USA*
[15]*Department of Physics, University of California, Berkeley, CA 94720, USA*
[16]*Institute for Gravitation and the Cosmos, The Pennsylvania State University, University Park, PA 16802, USA*
[17]*Campus of International Excellence UAM+CSIC, Cantoblanco, E-28049 Madrid, Spain*
[18]*Instituto de Astrofísica de Andalucía (CSIC), Glorieta de la Astronomía, E-18080 Granada, Spain*
[19]*Department of Physics, Ohio State University, 140 West 18th Avenue, Columbus, OH 43210, USA*
[20]*Institute for Astronomy, University of Edinburgh, Royal Observatory, Edinburgh EH9 3HJ, UK*
[21]*Department of Astronomy and Astrophysics, The Pennsylvania State University, University Park, PA 16802, USA*
[22]*Institute for Gravitation and the Cosmos, The Pennsylvania State University, University Park, PA 16802, USA*
[23]*Center for Cosmology and Particle Physics, Department of Physics, New York University, 4 Washington Place, New York, NY 10003, USA*
[24]*School of Physics and Astronomy, University of St Andrews, St Andrews, Fife KY16 9SS, UK*
[25]*Instituto de Fisica, Universidad Nacional Autonoma de Mexico, Apdo. Postal 20-364, Mexico City, México.*

This paper has been typeset from a TeX/LaTeX file prepared by the author.